Chemical and Charge Imbalance Induced by Radionuclide Decay: Effects on Waste Form Structure

Fuel Cycle Research & Development

Prepared for
U.S. Department of Energy
Waste Form Campaign
W. Jiang, R.M. Van Ginhoven,
D.M. Strachan
Pacific Northwest National Laboratories

March 2011
FCRD-WAST-2011-000070
PNNL-20312

Reviewed by:

Acting Director, Fuel Cycle Research and Development

Robert Price Date

Concurred by:

Director, AFCI Technical Integration Office

Phillip Finck Date

Approved by:

Deputy Assistant Secretary, Fuel Cycle Management

(AFCI Program Manager) Paul Lisowski Date

SUMMARY

Experimental

In this section, the experimental results for the Radiation Effects task are summarized. Results for $^{16}O^{+}$ and $^{90}Zr^{+}$ ion co-implanted $SrTiO_3$ (STO) single crystals were obtained from April 2010 to March 2011. In this study, STO was used as a model material to simulate a waste form for disposal of radioactive ^{90}Sr that decays to ^{90}Y and then ^{90}Zr by emission of β^- particles. Sequential $^{16}O^{+}$ and $^{90}Zr^{+}$ ion implantation at 550 K was performed and Zr and O atomic concentrations of up to 1.5 at% each in STO were achieved. Effects on the crystal structure, chemistry, and charge states in the implanted STO were studied. A number of analytical methods were employed to characterize the implanted STO, including secondary-ion mass spectroscopy, multiaxial ion-channeling analysis, transmission electron microscopy, X-ray diffraction, X-ray photoelectron spectroscopy, and Raman spectroscopy. The results show that, in contrast to the observed mobile Sr interstitials in STO, the implanted Zr does not diffuse noticeably during the ion implantation or thermal annealing up to 1423 K. A defect concentration was generated and accumulated in STO during the ion implantation, but the crystal structure was not rendered fully amorphous. Thermal annealing at 1273 K leads to a significant defect recovery at the surface with little recovery occurring at the damage peak, where a modest recovery occurs upon further annealing at 1423 K. The blocking ratio of Zr in STO, as observed along the <001> axis, is ~0.4 and ~0.5 after annealing at 1273 and 1423 K, respectively. Nearly all the implanted Zr species are not located exactly at the original lattice site due to structural distortion. A high density of dislocations was observed in the damage layer, where there were also Zr-containing superlattice structures and voids (or oxygen blisters). Results show that Zr is located at every other Sr site in the superlattice structure. Larger voids and dislocation loops exist beyond the damage layer. There was a minor phase with a tetragonal structure in the damage layer, where the implanted Zr was distributed. The tetragonal phase has the <001> axis parallel to that of the STO host. It survived thermal annealing at 1423 K with only a small decrease in the *c* value. Changes in chemical states or formation of new chemical bonding were not observed in this study because of the thin implanted layer and limited detection sensitivity. Discussion about the results and a general assessment of the model waste form are also provided in this report.

Theory

This section of this document contains a summary of the theoretical results for the portions of the Radiation Effects task, obtained from April 2010 to March 2011. The model system, SrTiO3 (STO), plus Zr and O, was investigated with ab inito calculations to determine structures, total energies, and electronic states. The calculations were carried out with density functional theory (DFT) in the Generalized Gradient Approximation (GGA) as described by Perdew, Burke and Enzerhof (1996) applied to a periodic supercell representation of STO. Significant effort was applied to selecting calculation sets that would enable comparison to the experimental results. Formation energies and structures were determined for the full spectrum of isolated intrinsic and O and Zr-related defects possible in the STO+Zr system.

The results show that the stable positions for the Zr interstitial (and Sr and Ti interstitials) are oriented along the <100 > <111> directions. The <100> defect is inserted halfway between two Sr atoms, and the <111> defect is a dumbbell type configuration, in which a Sr atom is displaced a small amount in the <111> direction, so that two metal ions are near the Sr lattice site. Each defect causes a change in the lattice parameters of STO. The presence of interstitial defects, particularly Zr, leads to a tetragonal distortion of the lattice. None of the investigated defects in the system are electrically active. All of the excess electrons from defects such as the Zr^{4+} substituted for the Sr^{2+}, or interstitial ions, are donated to the conduction band, and all the available acceptor levels are at the top of the valence band or lower. Interstitial Sr is qualitatively shown to be much mobile than interstitial Zr, at the preferred charge states for the defects. Quantitative verification of this result was beyond the scope of this study. In the

otherwise defect-free STO crystal, the additional charge introduced by the substitution of a Zr for a Sr atom occupies conduction band states with Ti3d electron orbital character. Charge distribution analysis confirms that the Zr^{4+} defect is charge compensated through corresponding reduction of Ti. The equilibrium location of Zr in the STO lattice depends on the system composition and the Fermi level or charge state of the defects. If there are available Sr vacancies, Zr will occupy the Sr site, whether or not charge effects are considered. If there are no vacancy sites available, the equilibrium state is a Zr in a Ti plus a Ti interstitial if the system is neutral (so that the Ti interstitial is donating 4 electrons to the conduction band). If the system is charged, so that all metal ions are in the preferred oxidation state, the Zr will occupy a Sr site, with a Sr interstitial. In this case, four conduction band electrons have been removed from the supercell, under the assumption that they will be compensated elsewhere.

CONTENTS

FIGURES

TABLES

ACRONYMS

CBM	Conduction Band Minimum
DFT	Density Functional Theory
EDS	Energy Dispersive X-ray Spectroscopy
EMSL	Environmental Molecular Sciences Laboratory
FIB	Focused Ion Beam
FWHM	Full Width at Half Maximum
GGA	Generalized Gradient Approximation
GIXRD	Grazing-angle Incidence X-ray Diffraction
HAADF	High-angle Annular Dark-field
HRTEM	High-resolution Transmission Electron Microscopy
LCAO	Linear Combination of Atomic Orbitals
LDA+U	Local Density Approximation (U is a parameter)
LMCC	Local Moment Counter Charge
McChasy	Monte Carlo Channeling Simulation
MD	Molecular Dynamics
MicroXRD	Micro-beam X-ray Diffraction
PIXE	Particle Induced X-ray Emission
PNNL	Pacific Northwest National Laboratory
RBS	Rutherford Backscattering Spectrometry
RBS/C	Rutherford Backscattering Spectrometry/Channeling Direction
SIMS	Secondary-ion Mass Spectroscopy
SRIM	Stopping and Range of Ions in Matter
STO	Strontium Titanate ($SrTiO_3$)
TEM	Transmission Electron Microscope or Transmission Electron Microscopy
TOF-SIMS	Time-of-flight Secondary-ion Mass Spectroscopy
TOPAS	Total Pattern Analysis Solution
XPS	X-ray Photoelectron Spectroscopy
Z	Atomic Number

1. INTRODUCTION – EXPERIMENT

Weilin Jiang
Contributors: Mark E. Bowden, Zihua Zhu, Przemyslaw Jozwik, Jacek Jagielski, Anna Stonert, Libor Kovarik, Bruce W. Arey, Ponnusamy Nachimuthu, and Guosheng Li

Operations in the nuclear power industry generate spent fuels that contain highly radioactive materials. The fission products of ^{235}U and ^{239}Pu have yields with masses ranging from 60 to 160 atomic mass units and peaked at 95 and 140 atomic mass units. Of the isotopes generated in these high-yield mass groups, ^{90}Sr and ^{137}Cs have high yields and long half-lives (29.1 and 30.2 y, respectively) (Lide 2003) relative to the other isotopes that are also generated. Thus, ^{90}Sr and ^{137}Cs are isotopes of concern in the nuclear waste stream from reprocessing of the spent fuels. The reprocessed wastes need to be immobilized prior to permanent disposal in a geological repository. Recent reports (Tollefson 2010) support an interim storage to allow time to develop a strategy for permanent disposal. Long-term storage or permanent disposal of nuclear wastes requires stabilization of the highly radioactive materials in a solid form that degrades very slowly over time, thereby limiting the release of radionuclides to the environment. Discovery and development of such forms for immobilization of nuclear wastes (Weber et al. 2009) are critical for proper management of existing and future spent fuels produced in the nuclear power plants. In the case of ^{90}Sr, the isotope decays to ^{90}Y by emission of a β^- particle with a half lifetime of 29.1 years and decay energy of 0.546 MeV, followed by a much faster, 2.28 MeV β^- decay (half life 64 hours) (Lide 2003) to stable ^{90}Zr . This β^- decay, changes the charge state from $^{90}Sr^{2+}$ to $^{90}Zr^{4+}$ with substantial heat production that can affect the structural stability of the host material and potentially lead to phase transformation, phase separation, or formation of new phases. In the work described here, strontium titanate ($SrTiO_3$ or STO) is used as a model material to simulate a waste form in which Sr decays to Zr. This material is readily available in single-crystal form, has outstanding physical and chemical properties, and is also well suited for theoretical investigations. To date, there have been not yet experimental studies of this simulated waste form reported in the literature. The data from the experimental study reported here may help understand various effects induced by ^{90}Sr decay on waste form properties and allow us to validate theoretical models and simulations. A part of the experimental data (Jiang 2011) reported here has been submitted for publication and the most recent ones, including TEM results, will be published in a later date.

2. EXPERIMENTAL METHODS AND MATERIALS

The single-crystal STO substrate (10 mm × 10 mm × 1 mm) with the (001) surface orientation used in this study was obtained from MTI Corporation (Richmond, CA). Ion implantation and sample characterization were performed in the Environmental Molecular Sciences Laboratory (EMSL) at the Pacific Northwest National Laboratory (PNNL). Ion implantation was conducted with a NEC 9SDH-2 pelletron 3.0 MV electrostatic tandem accelerator (Thevuthasan et al. 1999). An elevated temperature (550 K) for implantation was applied to avoid full amorphization of STO. To minimize the charge imbalance in the implanted STO, equimolar and overlapping implantation of ^{16}O and ^{90}Zr was employed. A beam rastering system was utilized to achieve uniform implantation over an area of 5 mm × 5 mm. Sample temperature was measured at the front surface through the use of a customized chromel-alumel thermocouple system. To produce a relatively wide plateau profile of the implanted Zr and O species for better characterization, computer simulations with the Stopping and Range of Ions in Matter (SRIM) code (Ziegler et al. 1985) were carried out, where the threshold displacement energies for Sr, Ti and O were chosen to be 80, 70 and 45 eV, respectively (Cooper et al. 2001; Smith et al. 2003; Smith and Zaluzec 2005; Zhang et al. 2005). As a result, ion energies and fluences for sequential implantation of O^+ and Zr^+ ions were selected, as given in Table 1. The sequences from 1-1 to 1-4 and from 2-1 to 2-4 in Table 1are referred to hereinafter as “Implantation 1” and “Implantation 2,” respectively.

Table 1. Experimental conditions for O^+ and Zr^+ ion co-implantation in $SrTiO_3$ at 550 K.

	Sequence	Ion	Energy, MeV	Total Fluence, 10^{16} ion/cm^2	Tilt, degrees
Implantation 1	1-1	O^+	3.00	2.00	60
	1-2	O^+	1.20	1.23	60
	1-3	Zr^+	2.75	2.00	7
	1-4	Zr^+	1.70	1.00	7
Implantation 2	2-1	O^+	3.00	6.00	60
	2-2	O^+	1.20	3.79	60
	2-3	Zr^+	2.75	6.00	7
	2-4	Zr^+	1.70	3.00	7

After Implantation 1, thermal annealing: 1273 K, 10 h in Ar.
After Implantation 2, first thermal annealing: 1273 K, 10 h in Ar and second thermal annealing: 1423 K, 10 h in Ar.
Implantation generates a plateau distribution of implants over the depths from 500 to 900 nm.
On the plateau, each of the O and Zr atomic concentrations is ~0.5 and ~1.5 at% for Implantations 1 and 2, respectively.

Implantation 1 results in ~0.5 at% each of O and Zr in the plateau region. After Implantation 1, the lattice disorder in the sample was characterized in situ at room temperature with 2.0 MeV He^+ Rutherford backscattering spectrometry (RBS) along the STO <001> axial channeling direction (RBS/C) at a scattering angle of 150°. The implanted sample was subsequently annealed at 1273 K for 10 h in flowing Ar. The RBS/C measurements were repeated for the annealed sample under the same conditions to study recovery of implantation damage. In addition, ex-situ grazing-angle incidence X-ray diffraction (GIXRD) was conducted with a Philips X'Pert multipurpose diffractometer with a fixed Cu anode operating at 45 kV and 40 mA. The depth profile of the implanted Zr was measured by use of a time-of-flight secondary-ion mass spectroscopy (TOF-SIMS), where O_2^+ and Bi^+ ion beams were used for sputtering and analysis, respectively. The depth scale was calibrated by measuring the crater depth with a Veeco Dektak 150 stylus profilometer.

A second implantation (Implantation 2) was conducted to increase each of the O and Zr concentrations to ~1.5 at% in the plateau region. Two parallel detection systems were employed for a simultaneous measurement of lattice disorder and implanted Zr with 3.0 MeV He^+ RBS/C and Particle Induced X-ray Emission (PIXE) under ion-channeling geometry (PIXE/C), respectively. The ion species and energy were selected to ensure a low PIXE background in the energy range of interest and to increase the RBS probe depth. For the PIXE measurements, a 20-μm thick Al foil was placed in front of the detector to reduce strong X-ray signals in the low-energy region from STO. The overall dead time during the data collection was maintained below 5%. Ex-situ thermal annealing was then performed at 1273 K (Table 1) and the measurements were repeated to study defect recovery and Zr location in the crystal structure. Further annealing was also conducted for the sample at 1423 K for 10 hours in Ar (Table 1). A number of characterizations followed, including GIXRD, micro-beam X-ray diffraction (MicroXRD), high-resolution X-ray diffraction (HRXRD), RBS/C, PIXE/C, TOF-SIMS and transmission electron microscopy (TEM). MicroXRD measurements were carried out with a Rigaku MicroMax 007HF system with a rotating Cr anode and a 2D image plate detector. High-resolution XRD was performed on a Panalytical MRD system that was equipped with a parabolic X-ray mirror and 4-bounce Ge (220) monochromator to produce a parallel Cu $K_{\alpha 1}$ beam. The ion channeling experiments (RBS/C and

PIXE/C) were performed along the STO <001>, <110> and <111> axes in the same implanted area. These orientations were initially mapped with the X-ray pole figure method and the data, together with the simulation results, are shown in Figure 1. The random orientation spectra were obtained at an off-axis orientation (polar = 7° relative to <001>, <110> or <111> axis) with rotating flip angles ranging from -3° to +3°.

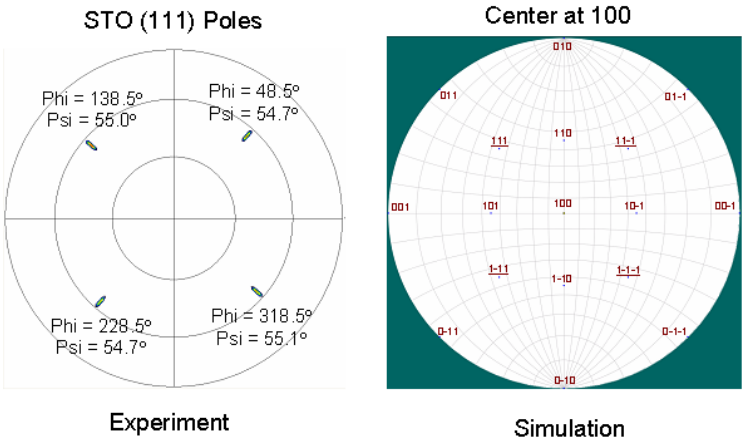

Figure 1. Pole figures of STO (111) from experiment and the corresponding low-index poles from simulation.

The RBS/C spectra have been analyzed with Monte Carlo channeling simulation (McChasy) (Nowicki et al. 2005). Overlapping Sr, Ti and O spectra made it impossible to accurately determine the atomic displacements on each sublattice in the implanted STO. The simulations were performed under the assumption of a random distribution of the atomic displacements with equal amount of Sr and Ti. The assumption of equal amounts was reasonable because nearly the same amount of relative disorder on the two sublattices in STO irradiated at 400 K with Au^+ ions was observed (Zhang et al. 2005). Evaluation of O displacements was subject to larger errors because its contribution to the RBS spectrum is located in the low-energy region with a relatively low intensity and its spectrum overlaps with higher-yield Sr and Ti spectra. The behavior of the implanted O and disorder on the O sublattice in STO is not discussed in this report. A cross-sectional thin specimen was prepared by use of focused ion beam (FIB, FEI Helios NanoLab 600), where 30 and 5 keV Ga^+ ions were used for cutting and polishing the sample, respectively, and 1 keV Ar^+ ions for nano milling. The specimen was examined for microstructures with a JOEL 2010 (spatial resolution = 0.2 nm) TEM at an operating voltage of 200 keV and FEI aberration-corrected Titan 80-300 TEM (spatial resolution = 0.1 nm) at 300 keV. X-ray Photoelectron Spectroscopy (XPS) and Raman Spectroscopy (Raman) were also used to study the chemical states and possible formation of new chemical bonds in the implanted layer at various steps during the ion implantation and thermal annealing.

3. RESULTS AND DISCUSSION – EXPERIMENT

3.1 Depth Profiles of Implanted Zr

Figure 2 shows the depth profiles of the sequentially implanted O and Zr predicted from the SRIM simulations. Under the implantation conditions (Table 1), both the overall O and Zr profiles are distributed with a plateau and are well overlapped each other over the depth. The implanted Zr in STO following Implantation 1 and thermal annealing at 1273 K was analyzed with TOF-SIMS. The same measurement was repeated for the sample after Implantation 2 and annealing at 1423 K. The concentration of the implanted ^{90}Zr in STO with depth is shown in Figure 3. The depth profile for Implantation 2 is normalized with a factor of 1/3 to that for Implantation 1. Also included in the figure is the result from SRIM simulation. Under the implantation conditions (Table 1),

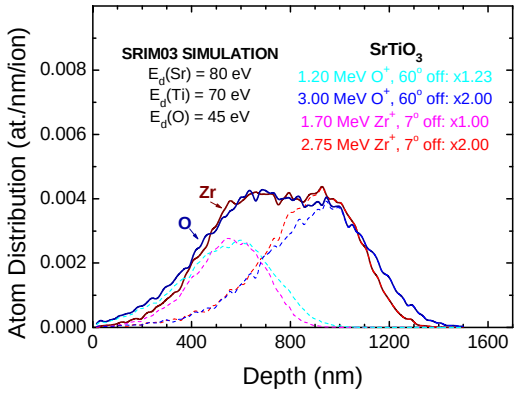

Figure 2. Depth profiles of ^{90}Zr and ^{16}O implanted into STO by SRIM simulation.

the Zr profile is distributed with a plateau ranging from 500 to 900 nm. For Implantation 1, the Zr concentration on the plateau is ~0.5 at%. Implantation 2 increases the concentration to ~1.5 at%.

In general, the experimental profiles are found to be in good agreement with the SRIM simulation, as shown in Figure 3. At larger depths, there are some differences, which could be attributed to the inaccurate SRIM depth scale caused by errors of Zr^+ ion stopping powers at low energies. The reasonably good agreement between the experiment and simulation suggests that there was insignificant Zr diffusion in STO during ion implantation at 550 K or on thermal annealing at 1273 K. From Figure 3, the two normalized depth profiles of ^{90}Zr are virtually identical, indicating that there is an insignificant diffusion of ^{90}Zr during Implantation 2 at 550 K or subsequent annealing up to 1423 K for 10 hours. The results are in contrast to significant diffusion of implanted Si (Sakaguchi et al. 2001), Eu (Ramos et al. 1995), and Pb (Cherniak 1993) in STO during thermal annealing. Instead of freely migrating interstitials, the implanted Zr could be chemically bonded in the STO structure that tends to immobilize ^{90}Zr (see below). An area without implanted ions was also analyzed with the TOF-SIMS, which shows a flat distribution of ^{90}Zr isotope as an impurity with a concentration of ~2 orders in magnitude less than that on the plateau (data not shown). This low level of concentration is also exhibited in Figure 3 at depths larger than 1300 nm.

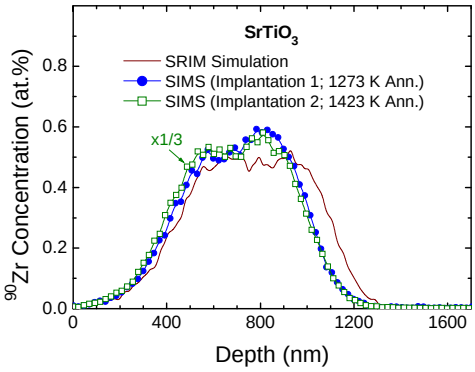

Figure 3. Depth profiles of ^{90}Zr in STO by SIMS experiment. Also included is the SRIM simulation result.

3.2 Atomic Displacements and Extended Defects

In-situ 2.0 MeV He^+ RBS/C for STO after Implantation 1 was performed at room temperature along the STO <001> axis. The channeling spectra for the as-implanted sample and after thermal annealing at 1273 K are shown in Figure 4. Also shown in the figure are a RBS/C spectrum and a random spectrum from an unimplanted area. The depth scale, shown on the top axis, is obtained from the SRIM database (Ziegler et al. 1985) with a surface energy approximation (Chu 1978). The minimum yield, χ_{min}, determined from the channeling and spectra for STO prior to implantation, is ~2.3% (Figure 4), indicating that the STO had high crystalline quality prior to ion implantation. Amorphous and essentially defect-free STO are defined by the random and channeling spectra from the unimplanted area, respectively. The disordered crystal has a backscattering yield between these two limits. Apparently, a high defect concentration is produced after Implantation 1 and considerable defect recovery occurs in the surface region after thermal annealing at 1273 K. Accurate determination of the defect concentration in the entire implanted depth region is challenging because of the spectrum overlap. However, in the surface region where ion dechanneling caused by beam angular divergence is negligible, the relative disorder on the Sr sublattice can be estimated by (Jiang 2001)

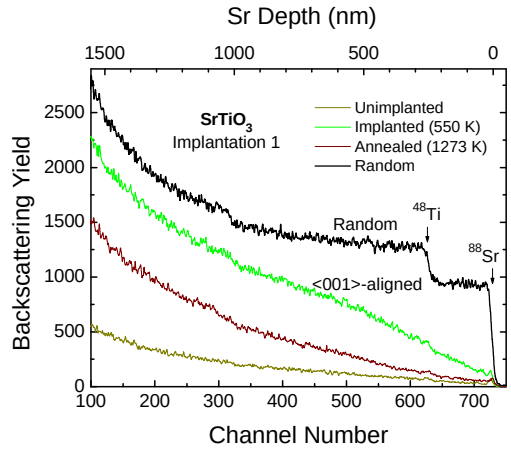

Figure 4. Random and <001>-aligned spectra of 2.0 MeV He^+ ion RBS for STO before and after Implantation 1 and thermal annealing at 1273 K.

$$n_d = \frac{(h - \chi_R)}{(1 - \chi_R)} \tag{1.1}$$

where h and χ_R are the yield ratios of the aligned spectra for the implanted and unimplanted samples to the random spectrum at the surface, respectively. According to Equation (1.1), the relative Sr disorder in the as-implanted sample near the surface (depth = 30 – 50 nm) is ~10%. The disorder level is expected to be a few times higher at the damage peak. The data also suggest that the material is not completely amorphized throughout the entire thickness of the implantation layer. Subsequent to the thermal annealing, the relative Sr disorder near the surface is reduced to ~3%, but complete recovery of the damage does not occur even at the surface, where the defect concentration is low.

After adding O^+ and Zr^+ fluences in Implantation 2 at 550 K, the defect concentration was reanalyzed with 3.0 MeV He^+ RBS/C for a larger probe depth. The results from the RBS/C along the STO <001> axis, together with the spectrum from a completely randomized implantation, are shown in Figure 5. Note that although only Coulomb scattering or Rutherford scattering occurs for sublattices Sr and Ti, there is an enhanced backscattering yield for the O sublattice from nuclear resonance. The results from McChasy simulations are also included in Figure 5. The slightly higher yield around the Ti surface edge in the random spectrum is from the implanted Zr contribution. The relative Sr disorder at the surface increases as a result of Implantation 2 and decreases after thermal annealing at 1273 K, as expected. Further annealing at 1423 K leads to a slight recovery in the deeper region, as shown in Figure 5.

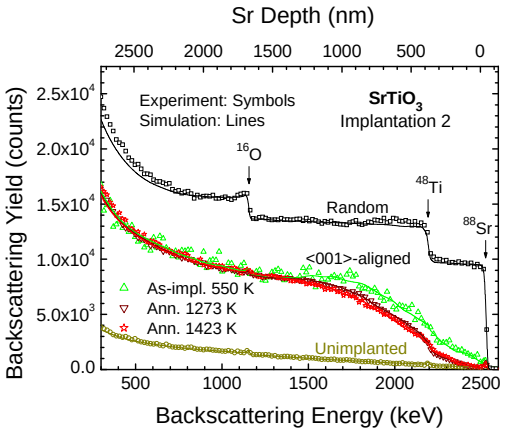

Figure 5. Random and <001>-aligned spectra of 3.0 MeV He^+ ion RBS/non-RBS for unimplanted STO and after Implantation 2 and thermal annealing at 1273 and 1423 K.

The percentage of Sr displacements obtained from McChasy simulations is shown in Figure 6. The normalized result from SRIM simulation is also included in the figure as indicated by a dashed line. For the as-implanted sample, there is a rather symmetric distribution of the Sr displacements with a percentage of ~28% at the damage peak (~700 nm deep) and a full width at half maximum (FWHM) of ~900 nm. Compared to the profile, SRIM result shows a small peak shift to a smaller depth, which could be again attributed, in part, to the inaccurate database in SRIM. It is also likely that some of the Sr interstitials in the crystal structure diffuse into the deeper region during ion implantation at 550 K. A previous study (Thomas et al. 2007) of molecular dynamics (MD) simulations on STO has predicted that Sr interstitials are very mobile; they migrate linearly along the <001> direction with interstitial migration energy of only 0.3 eV. In addition, defect clusters (such as dislocation loops) are expected to form in the implanted layer and structural distortion could occur (see below); those defects can defocus the beam and lead to a higher dechanneling yield at a greater depth. Upon annealing of the implanted sample at 1273 K for an extended time (10 hours), significant recovery of the implantation damage at the surface is observed, which is consistent with annealing after Implantation 1 (Figure 4). However, the level of disorder at the damage peak remains unchanged. At larger depths, damage level becomes higher and a long tail appears in the damage profile. Possible reasons are again interstitial diffusion and/or presence of defect clusters in the crystal structure. The density and size of the defect clusters could change as a result of the thermal annealing at 1273 K. Further annealing at 1423 K results in a modest recovery at the

damage peak; however, there is virtually no more recovery of defects in the near-surface region. The damage profile becomes more skewed and a longer tail appears. Interstitial diffusion and/or beam defocusing could be responsible for the profile.

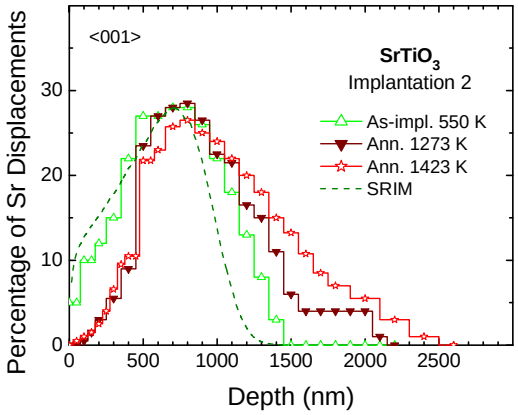

Figure 6. McChasy simulation results of atomic displacements on the Sr sublattice in STO observed along the <001> axis after Implantation 2 and thermal annealing at 1273 and 1423 K. Also included is the result from SRIM simulation.

Multiaxial channeling RBS/C analysis of the sample after Implantation 2 and annealing at 1423 K was performed at the same spot along the STO <001>, <110> and <111> axes by tilting and rotating the sample to those orientations. The percentage of Sr displacements is shown in Figure 7 as a function of depth. Similar multiaxial channeling studies have been reported for different polymorphs of SiC (Jiang et al. 2009; Jiang 2001; Zhang et al. 2004) to obtain information about defect configurations. Apparently, the peak damage observed along the <110> axis is much higher than that along either <001> or <111>, indicating that some of the displaced Sr atoms are well aligned with the <001> and <111> axes in the damage peak region. The results are consistent with an MD prediction (Thomas et al. 2007) that Sr forms a split interstitial along <100> or its equivalent axes. From this study, it is evident that this type of defects is stable to high temperatures (1423 K). Similar split interstitials along <111> could also exist and need to be investigated theoretically. It is also interesting to notice that for the same damage state, the concentration of the Sr displacements appear to be higher when observed along the <111> direction than along <001> or <110> at large depths (> 1.3 µm) beyond the implantation damage. The behavior could be associated with the location and migration path of Sr interstitials in STO and is consistent with MD simulations (Thomas et al. 2007).

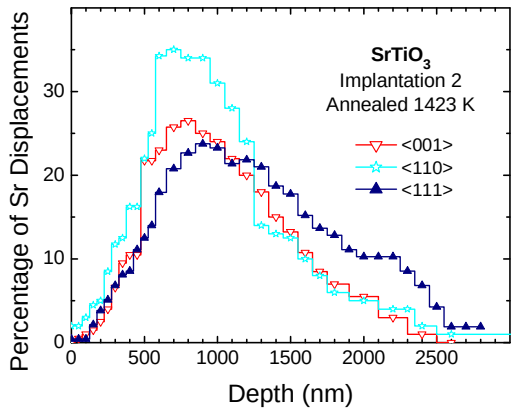

Figure 7. McChasy simulation results of atomic displacements on the Sr sublattice in STO after Implantation 2 and annealing at 1423 K, observed along the <001>, <110> and <111> axes.

In addition, a cross-sectional TEM was also used to study the microstructures and extended defects in the STO after Implantation 2 and thermal annealing at 1423 K. Figure 8 shows a low-resolution bright-field TEM image (from JOEL 2010), where different microstructures are exhibited over the depth region. The Pt and C layers were deposited prior to FIB preparation of the TEM specimen for protection of the sample surface from sputtering or irradiation damage. There are low-density dislocations near the sample surface (within a depth of 460 nm), followed by a damage layer between 460 nm and 1 µm, where a much denser dislocations exist. The depth scale is in a good agreement with the data shown in Figure 6, indicating that volume swelling in the implanted region is not very significant after the thermal treatment. At larger depths beyond the damage layer, dense dislocation loops (~1.2 µm deep) and large voids of tens of nanometers in size (~1.4 µm deep) are observed. Formation of the dislocation loops could be attributed to interstitial/vacancy diffusion and thermal annealing at high temperatures. The voids are clearly faceted along the energetically favored (001) plane or its equivalent planes. Similar voids of a few nanometers in size are also observed near the STO surface, as shown in the inset of Figure 8. These voids could nucleate at the end of dislocations by trapping mobile vacancies and grow into larger sizes. Oxygen diffusion in STO under the experimental conditions is likely and formation of oxygen-filled blisters could

occur, which would lead to a void-like structure after rupture and reconstruction of the inner surface morphology. There are no observable dislocation loops at depths larger than 1.6 µm.

3.3 Location of Implanted Zr

The location of the implanted species and its substitutional fraction can be conveniently investigated for heavy implants in light single-crystal substrates with conventional RBS/C. However, RBS cannot resolve spectra of implanted species with a comparable or smaller atomic number (Z) in medium to heavy substrates. Unfortunately, the latter case applies to this study where implanted ^{90}Zr cannot be resolved from the ^{88}Sr in the RBS spectra. To study Zr in STO, we explored the use of PIXE/C.

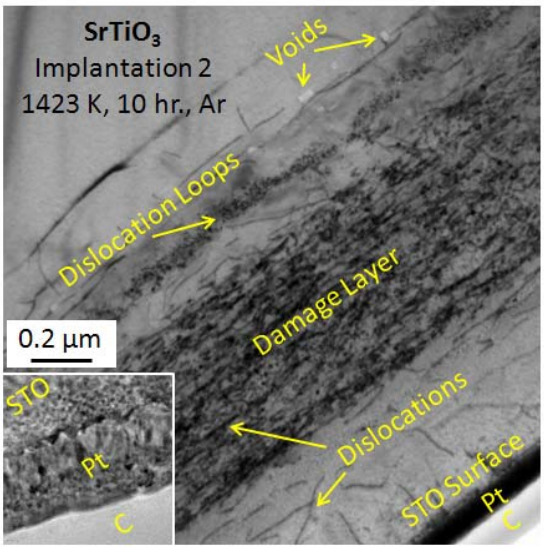

Figure 8. Low-resolution bright-field TEM image of STO after Implantation 2 and annealing at 1423 K.

Figure 9 shows typical random PIXE spectra for ZrO_2 and STO single crystals with 3.0 MeV He^+ ion beam. Compared to conventional MeV H^+ PIXE, MeV He^+ PIXE produces a lower background because of less bremsstrahlung. From Figure 9, the intensity of the characteristic X-ray emission from STO is relatively high below 16 keV, rendering this energy range of no use in the detection of Zr at low concentrations. However, above 17 keV, STO background is low. On the other hand, Zr K_β at ~17.7 keV, consisting of Zr $K_{\beta1}$ (E = 17.67 keV; relative intensity = 15%), Zr $K_{\beta2}$ (17.97 keV; 3%) and Zr $K_{\beta3}$ (17.65 keV; 8%), has reasonably high intensity (Figure 9). These characteristic X-rays were used to quantify Zr in STO.

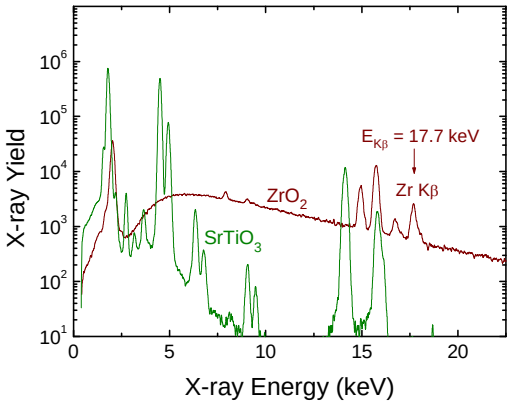

Figure 9. Random spectra of 3.0 MeV He^+ PIXE for yttrium-stabilized ZrO_2 and STO substrates. The Zr K_β lines at E = ~17.7 keV are used for analysis of Zr in STO of this study.

Figure 10 shows 3.0 MeV He^+ ion PIXE/C and random spectra for an unimplanted STO and the STO after Implantation 2 and annealing at 1273 and 1423 K. The data were recorded along the STO <001>, <110> and <111> axes at the same time when RBS/C spectra were collected (e.g., Figure 5 for the <001>-aligned spectra). Since PIXE does not have depth resolution, the Zr K_β peak originated from the entire thickness of the implanted region, primarily from 500 to 900 nm (Figure 3). The integrated counts of the peak are proportional to the total number of Zr seen by the incident He^+ ions. From Figure 10a, the peak intensity of the random spectrum is higher than that of the <001>-aligned spectrum after annealing at 1273 K, indicating that some of the Zr atoms are aligned with or shielded by the <001> atomic row. Further annealing at 1423 K led to a small decrease in the peak intensity of the aligned spectrum. In contrast, the <110>- and <111>-aligned spectra for annealing at 1423 K shown in Figure 10b and c, respectively, have the same peak areas as those of their corresponding random spectra within the statistical fluctuation (~5%). The data suggest that nearly all the implanted Zr in STO are visible along the <110> or <111> axis.

In general, when an impurity concentration is low (1 at%), channeling properties of the host crystal will not be noticeably affected by the presence of the impurity. The impurity atoms will follow the same angular dependence as the host atoms if they are located at substitutional sites. For a mixed site case where a portion of impurities is located on the substitutional site and the remainder occupies a random distribution of sites, a first-order estimation of the substitutional fraction, *S*, can be expressed as (Feldman et al. 1982):

$$S = \frac{(1-\chi_i)}{(1-\chi_h)} \qquad (1.2)$$

where $\chi_i = A_i(a)/A_i(r)$ and $\chi_h = A_h(a)/A_h(r)$. The symbols $A_i(a)$ and $A_i(r)$ denote the total peak areas of impurity (i) in the aligned (a) and random (r) spectra, respectively, while $A_h(a)$ and $A_h(r)$ corresponds to the integrated areas of the host (h) in the aligned and random spectra. This concept has been successfully applied in various cases, including a previous study of Sn^+ ion implanted rutile (Fromknecht et al. 2000). In this study, Zr impurity concentration in STO is relatively low (1.5 at%) and the half width of the angular yield curve for Sr in STO remains virtually unchanged after Implantation 2 and annealing at 1273 or 1423 K. However, Zr distribution in the crystal structure significantly deviates from the presumed mixed sites. Since Equation (1.2) is only valid for the special case, the value of *S* cannot be interpreted as a substitutional fraction in this study. For a more general distribution of implants, the *S* in Equation (1.2) may be viewed as an overall fraction blocked by an atomic row. A blocking ratio, taken the same form of Equation (1.2), may be defined as a fraction of impurity atoms that are blocked by an atomic row due to axial channeling. The blocking ratio ranges from 0 for complete visibility to 1 for complete blocking. For an unknown distribution of implants, substitutional fraction needs to be estimated from a multiaxial channeling study.

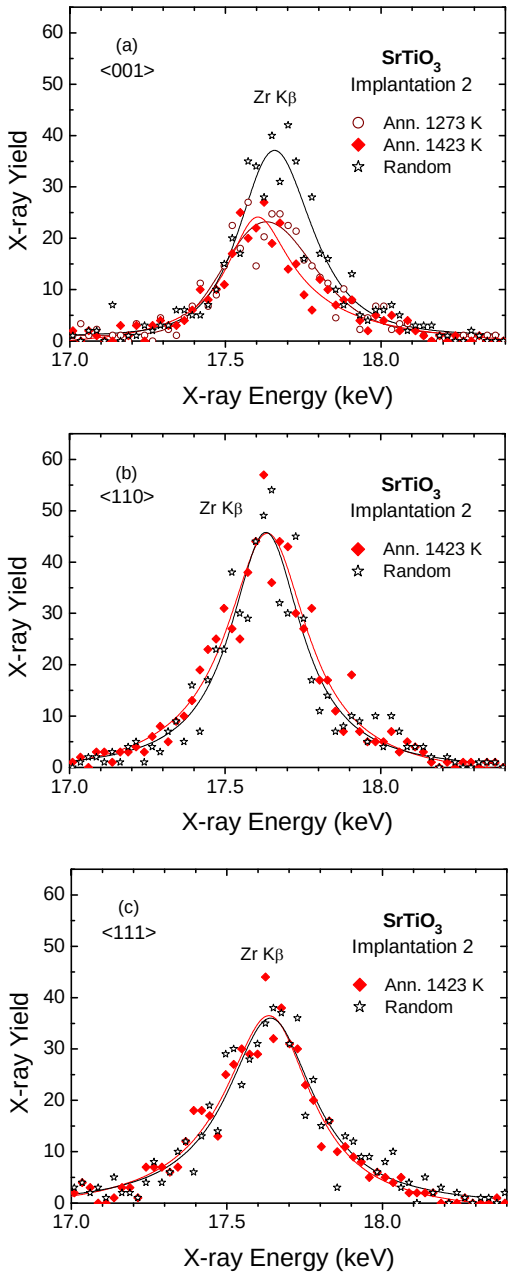

Figure 10. Random and (a) <001>-, (b) <110>-, and (c) <111>-aligned spectra of 3.0 MeV He^+ PIXE for STO after Implantation 2 and annealing at 1273 and 1423 K.

The channeling and random spectra for the host Sr sublattice have been obtained from McChasy simulations. From Figure 10a, the overall blocking ratio of Zr in the implanted region along the STO <001> axis is estimated to be ~40% after annealing at 1273 K and ~50% after further annealing at 1423 K. The remainder of the implanted Zr is located at positions visible along the <001> axis. Similarly, from Figure 10b and c, the overall blocking ratio is virtually zero along the <110> or <111> axis. If a lattice atom (Sr or Ti) is substituted for a Zr atom in the STO structure, the Zr atom will be blocked by any of the major crystallographic axis. The fraction of substitutional Zr, ranging from 0 (no substitution)

to 1 (complete substitution), is at most the minimum value of the blocking ratios observed along these channeling directions, which is about zero. Thus, nearly all the Zr implants in the STO are not located exactly at the original lattice site, in part, due to the structural distortion in the damage layer (see below).

Figure 11 shows high-resolution high-angle annular dark-field (HAADF) TEM images of the same sample inside the damage layer (from Titan 80-300). In general, STO crystal structure is largely maintained in the damage layer except for some disordered regions. Small voids (darker zones) and Zr-containing structures (brighter zones) of a few nanometers in size are observed, as indicated in the figure. Energy dispersive X-ray spectroscopy (EDS) was used to confirm the presence or absence of Zr in different zones (data not shown). Calculated reciprocal lattice of the Zr-containing structure shows extra spots as compared to that of pure STO, as shown on the left side of Figure 11. The atomic-resolution image on the right panel of Figure 11 clearly shows Sr (darker) and Zr (brighter) locations, while Ti atoms, located in the center of the Sr square, are not visible because of specimen thickness. The data suggest that Zr is distributed at every other Sr site and is arranged alternatively with the regular Sr lattice, as the model on the upper right corner illustrates. This atomic configuration constitutes a superlattice structure with a lattice parameter (~0.78 nm) of about twice as large as for STO. The structure explains the extra dim spots in the reciprocal lattice space, which corresponds to (001), etc. of the superlattice structure, while its (002) spot overlaps with (001) of the pure STO. However, it still remains to be investigated whether and how the charge around the Zr is well balanced. Possible configurations for the charge balance include O^{2-} interstitials, doubly charged vacancies and a reduced Ti charge state. It should be noted that although the data in Figure 11 suggests substitution of Zr for Sr in the superlattice structure, the substitutional Zr is not located at the original Sr site in perfect STO due to lattice distortion (see below). Ion channeling is extremely sensitive to detect atomic displacements, as has been previously demonstrated for the Si and C displacements in SiC (Jiang 2001). Therefore, the TEM data are complementary to the PIXE/C data in Figure 10, which are also consistent with the XRD data below.

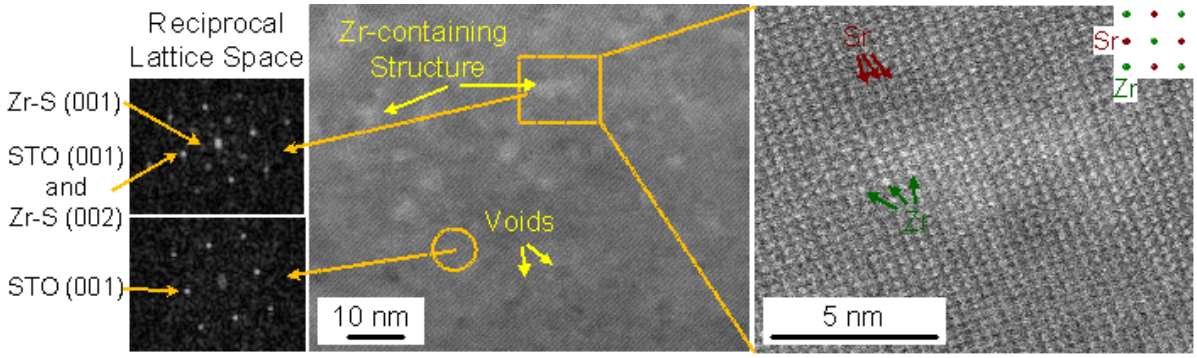

Figure 11. High-resolution HAADF TEM images of the damage layer in STO after Implantation 2 and annealing at 1423 K. The reciprocal lattice spots of a Zr-containing structure and the pure STO as well as a model of Zr locations are also shown. Zr-S stands for Zr-containing structure.

3.4 Formation of New Phases

MicroXRD was used to characterize both the implanted and unimplanted areas. The data for STO after Implantation 2 and annealing at 1273 K are shown in Figure 12a. While the unimplanted area shows a single-phase STO diffraction pattern (cubic phase with a = 0.3905 nm) as expected, the implanted area shows a double-peak structure for all the diffraction peaks. Data fitting with the "hkl phase" option of TOPAS (Bruker AXS) was performed, where the peak shapes were consistent across the 2θ range with positions determined by unit-cell parameters. The fitting results are shown in Figure 12a and b suggest that the small peaks originate from a minor phase that has a tetragonal structure with a = 0.3905 nm and c = 0.3968 nm. All the fine features in the pattern can be well fitted with the lattice parameters. As an example, Figure 12b illustrates such a data fit in an expanded view of the (220) peak. In addition, the

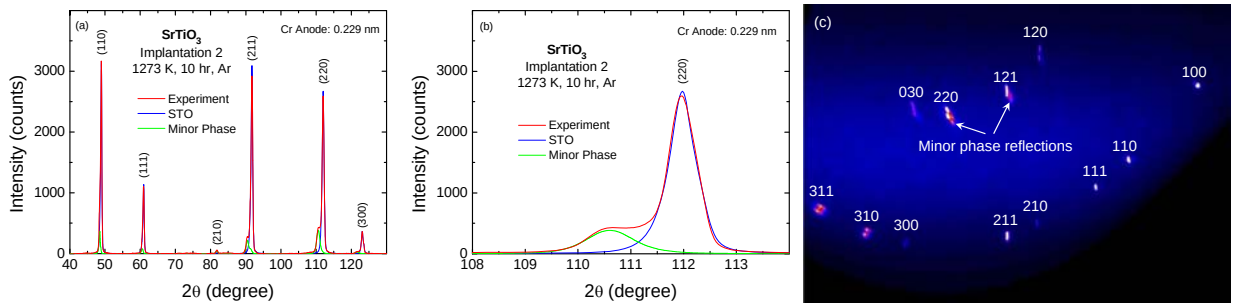

Figure 12. (a) MicroXRD pattern and fitting result for STO after Implantation 2 and annealing at 1273 K. (b) Expanded view of (220) reflection and the minor tetragonal phase from the data fitting. (c) Diffraction image for the same sample, where minor-phase reflections are indicated.

diffraction image from the MicroXRD exhibits bright spots instead of arcs as shown in Figure 12c, indicating that that the observed minor phase is not randomly oriented in STO. The double or elongated spots in the figure are artifacts, arising from a small tilt in mounting the sample. The weak reflections from the minor tetragonal phase are observed close to the STO (220) and (121) reflections, as indicated in the figure. The non-polycrystalline nature of the minor phase is confirmed by GIXRD for the sample, as shown in Figure 13, which does not show multiple diffraction peaks. Furthermore, symmetric scans (data not shown) only show out-of-plane reflections, indicating that the tetragonal structure is epitaxially <001>-oriented with the STO host. Generally, structural defects (interstitials, interstitial clusters, vacancies, etc.) can induce lattice expansion or contraction along the normal of the free surface, which leads to peak shift and broadening (Jiang 2007). The observed minor phase is believed to be associated with lattice expansion along the *c* axis in the implantation layer where Zr is located. Since ~40% of the implanted Zr are aligned with the <001> axis (Figure 10a), they are expected to be a part of the constituents of the tetragonal structure. The chemical bonding of Zr in the structure is consistent with the SIMS results (Figure 3) that suggest that the implanted Zr is not very diffusive in STO even at 1423 K.

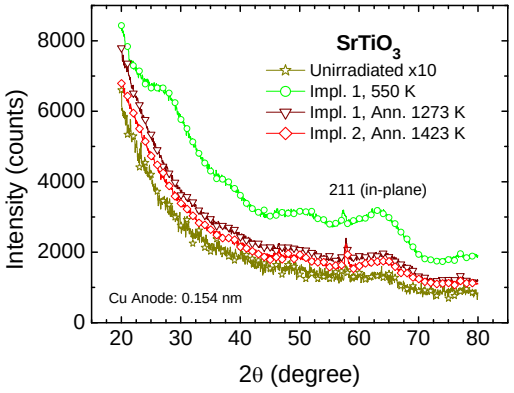

Figure 13. GIXRD patterns for STO before and after ion implantation and thermal annealing.

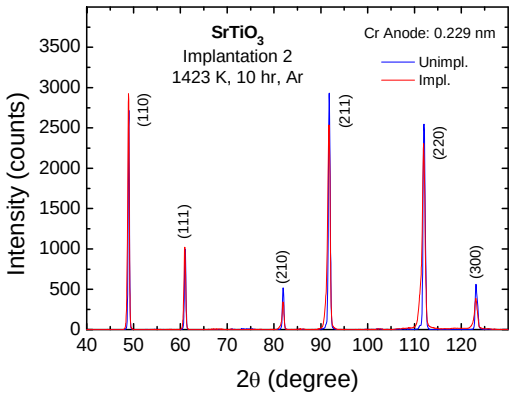

Figure 14. MicroXRD patterns for the unimplanted STO and the sample after Implantation 2 and annealing at 1423 K.

Thermal behavior of the minor phase also has been studied with MicroXRD analysis, and the data for annealing at 1423 K is shown in Figure 14. Compared to unimplanted STO, the implanted sample exhibits similar diffraction peaks with fine structures as those shown in Figure 12a. Similar data fitting suggests that the structure of the minor phase is tetragonal with $a = 0.3905$ nm and $c = 0.3933$ nm. This corresponds to a lattice expansion of 0.7% and shrinkage of 0.9% along the *c* axis relative to the STO prior to implantation and the tetragonal phase observed after annealing at 1273 K (Figure 12a), respectively. Analysis of the sample with HRXRD for symmetric scans was also performed. The data

are shown in Figure 15, including patterns for both the implanted/annealed and unimplanted areas. From Figure 15, it is clearly seen that a shoulder-like peak is attached to each of the strong STO peaks for the implanted/annealed sample, while the unimplanted STO only shows single peaks. This indicates that the minor phase survives the high-temperature annealing with only a small change in the *c* lattice parameter. This small change could be associated with structural relaxation. The tetragonal structure should be associated with the observed Zr-containing superlattice structure, as shown in Figure 11.

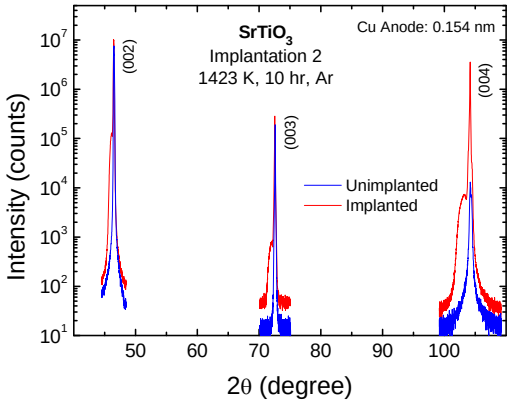

Figure 15. HRXRD patterns for the unimplanted STO and the sample after Implantation 2 and annealing at 1423 K.

3.5 Chemical Bonding

Raman scattering was attempted to study possible formation of new chemical bonding. To reduce photoluminescence, an excitation wavelength of 514.5 nm was used. At various steps during the implantation and thermal annealing cycles, the samples were analyzed with Raman. As a typical example, the results for the unimplanted sample and the sample after Implantation 2 and annealing at 1273 K are presented in Figure 16. The overall spectrum shape for the unimplanted and implanted samples is identical, indicating that signals from the implanted Zr are not resolvable. All the observed features, including convoluted peaks, originate from the STO single crystal (Nilsen and Skinner 1968). Since the background is high, any real signal associated with the Zr chemical boding is submerged. This is mainly because the implanted layer is thin (less than 1 μm) with a low Zr concentration (~1.5 at%) and the penetration length of the laser beam is much larger in the crystal. The dominant volume that contributes to the spectrum intensity is from STO. Unless signal-to-noise ratio is significantly improved, the detection limit is insufficient to resolve the Zr signal from STO. Further attempts could be performed for a higher Zr concentration with grazing-angle incidence.

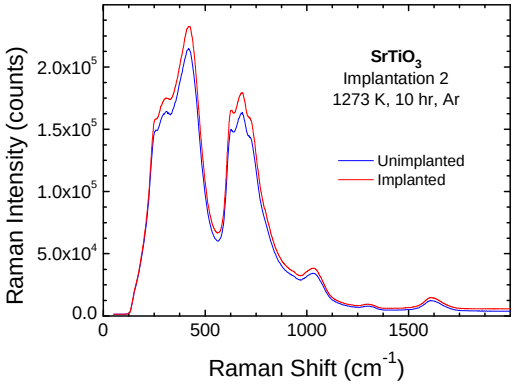

Figure 16. Raman spectra for unimplanted and implanted STO after thermal annealing.

3.6 Charge State

These samples were also analyzed with XPS in an attempt to examine any change in the chemical state of the implanted and host atoms. Sample surface, an edge area and a freshly cleaved cross-section were probed with an X-ray beam of 100 μm in spot size. Since the implanted Zr is mainly distributed at depths of 500 – 900 nm, no observable Zr spectrum was found with the surface-sensitive XPS (probing depth on the order of a few atomic layers to a few nm). While ion sputtering of the surface is possible to remove the surface layer covering Zr, the process would result in preferential sputtering of oxygen and an amorphous surface. Consequently, the chemistry measured would then be different from what it was before sputtering. The measurement from an edge was also not ideal since the Zr chemistry could be different in the bulk. For this reason, the sample was cleaved in air and quickly put it into the XPS vacuum chamber (within 5 minutes). Half of the beam spot centered close to the sample surface edge was used for the measurement. A survey spectrum from the cleaved cross-section containing the implanted layer (Implantation 2 and 1423 K anneal) is shown in Figure 17. The main contribution to the spectrum intensity is from host atoms (Sr, Ti and O). A small amount of surface carbon is also observed, which is typical for XPS even in ultrahigh vacuum. The binding energy for Zr $3d_{5/2}$ and $3d_{3/2}$ peaks is around 180

eV, which is near the strong Sr $3d_{5/2}$ and $3d_{3/2}$ peaks. No resolvable Zr peaks are observed in the survey spectrum.

More detailed scans around the Zr peak region were also performed for the unimplanted and implanted areas. The XPS normalized spectra (displaced from one another for clarity) are shown on the right hand side of Figure 18. Both areas do not show Zr 3d peaks. This is also the case after the cross-section was sputtered for a few nanometers with 2 keV Ar^+ ions (Figure 18). The reason may be the small amount of Zr in the detection area. Within the beam spot, only ~1% of the area has Zr, where the concentration is ~1.5 at%. Thus, there is only ~0.015 at% of Zr in the detection area. In addition, the Zr signal is located in a part of the spectrum with relatively high background (Figure 17). Likewise, changes in Ti $2p_{3/2}$ and $2p_{1/2}$ are also not observed for the implanted sample before sputtering. However, the Ti $2p_{3/2}$ peak exhibits a small tail on the high-energy side after sputtering of the cleaved surface, indicating a reduction of the Ti^{4+} charge state (Figure 18 on the left hand side). This behavior is expected because of the preferential sputtering of oxygen and amorphization of the surface. This high-energy tail becomes more prominent when sample is tilted and more surface region is probed. The feature could be useful in future efforts to study changes in the charge states. To increase the probabilities for resolving Zr 3d peaks and studying Ti charge states, the X-ray beam-spot size needs to be further decreased, which leads to an increase in the signal-to-noise ratio.

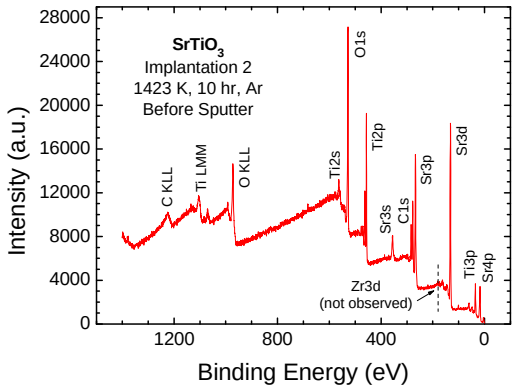

Figure 17. Survey XPS spectrum for STO after Implantation 2 and annealing at 1423 K.

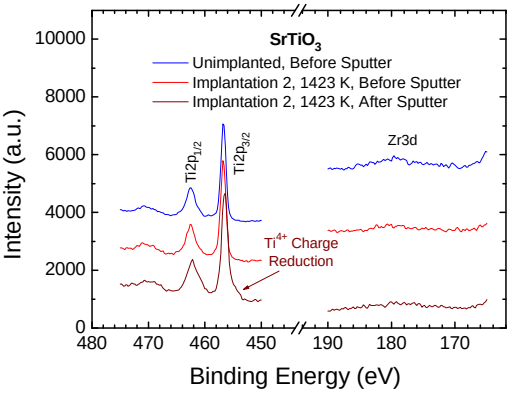

Figure 18. Ti 2p and Zr 3d XPS spectra for unimplanted and implanted STO before and after 2 keV Ar^+ ion sputtering.

4. GENERAL DISCUSSION AND ASSESSMENT – EXPERIMENT

Single crystal STO has a high melting point (2353 K), high thermal stability, and high mechanical strength. It can be readily amorphized under ion irradiation at room temperature (Thevuthasan et al. 2003; Zhang et al. 2005). The critical temperature for amorphization of STO is ~370 K (Zhang et al. 2005), above which full amorphization does not occur and only a disordered crystalline structure is produced even under intense ion or electron irradiation. Formation of defect clusters, including dislocation loops, in the crystal structure is expected during high-temperature, high-dose implantation. Once such a disordered structure is formed, it is difficult to fully recover the perfect crystal.

There are two major factors that affect structural stability, self-irradiation induced defects and charge-imbalance effects. In both the first and second β^- decay processes for ^{90}Sr, the daughter nuclei of ^{90}Y and ^{90}Zr are not expected to be displaced from their lattice sites upon emission of electrons. This is because the kinetic energy imparted to the nuclei is too small. Even for emission of an electron at the highest possible energy (2.28 MeV) in the second decay, the ^{90}Zr recoil receives only ~6 eV. The excess energy

is eventually converted to heat. However, self-irradiation of the energetic electrons can induce atomic displacements in the elastic collision process, especially for the high-energy electrons emitted from the second decay (^{90}Y to ^{90}Zr), where the most probable energy is 760 keV (Jiang 2010). Due to heat production from the decays, the material temperature could be well above room temperature, depending on storage environments, such as cooling or ventilation conditions. If the material temperature is below the critical temperature for amorphization, the crystal under self-electron irradiation can be fully amorphized at a critical dose due to defect accumulation and interaction. The lower the temperature is, the higher the disordering rate is. It should be noted that, compared to ion irradiation, the critical temperature for electron irradiation is generally lower. If the material temperature is at or above the critical temperature, more irradiation-induced point defects, including close Frankel pairs, are recovered simultaneously and the crystal will not become fully amorphous. However, some interstitials and vacancies can cluster and form extended defects that are thermally stable to high temperatures.

In addition, chemical effects are also expected to play a key role in the structural evolution. As β^- decays proceed, a change in the charge state from $^{90}Sr^{2+}$ to $^{90}Y^{3+}$ and then to $^{90}Zr^{4+}$ occurs. Although substitution of Zr^{4+} (ionic radius = 72 pm) for six-coordinated Sr^{2+} (118 pm) is possible, the charge imbalance and the large difference in their ionic radii make the presumed structure less stable. It is still yet unknown how stable the presumed perovskite structure of $ZrTiO_3$ is at high temperatures and whether decomposition of the crystalline phase can take place under self-irradiation. Certainly, the resulting structure is more susceptible to electron irradiation because of the charge imbalance. To avoid the charge effect, substitution of Zr^{4+} for Ti^{4+} could take place. However, such a simple substitution is not energetically favored and may be thermally unstable because the ionic radius of Zr^{4+} is considerably larger than that of Ti^{4+} (60.5 pm). Calculations performed in this project indicate that, in the absence of interstitials, substitutional Zr on the Sr site is more stable than the Ti site (see below). In a recent theoretical study of ^{90}SrO, Jiang (2010) predicted formation of ^{90}ZrO in a CuTi-structured phase, which is mechanically and dynamically stable and has a small driving force to decompose into ZrO_2 and Zr_2O. To achieve a more stable structure, addition of charge-compensating ions to the model system seems to be one of the reasonable approaches.

In the experimental study reported here, we chose O^{-2} ions for charge compensation in Zr-incorporated STO structure. A tetragonal structure is observed, whose <001> axis is parallel to that of the host crystal. The implanted Zr species are distributed in this depth region and long-range diffusion of Zr does not occur even at high temperatures (1423 K). Tight chemical bonding of Zr in the structure is expected. We have also showed that the observed tetragonal phase is stable to high temperatures (1423 K). There is evidence that Zr tends to substitute for Sr at every other lattice site. Substitution of Zr for Ti in STO is not observed. However, it still remains to be investigated whether and how the charge around the Zr is well balanced and what role the surrounding defects may play. Chemical imaging at the scale of atomic resolution coupled with *ab initio* calculations and modeling are required to address these questions. These studies are needed to address the effects of ^{90}Sr to ^{90}Zr decay on the overall chemical durability of a crystalline host for ^{90}Sr. The material studied here is a stand-in for the actual Sr-bearing phase that might be used in the immobilization of ^{90}Sr, but similar effects as observed in this study are likely unless the solid contains adequate charge-compensating ions. While O^{-2} ions could be a good candidate for charge compensation in the model waste form of this study, it is not yet clear whether there are more effective ions for the system. For example, elements with more availability of different oxidation states could be substituted for one or more of the constituent elements. In addition, if the superlattice structure observed from this study is proven to be a favored waste form, stable Sr isotopes also need to be added.

5. INTRODUCTION – THEORY

Renee M. Van Ginhoven and John Jaffe

This effort is intended to develop validated atomic-level simulation models for the effects of chemical change and charge imbalance that are induced by radionuclide decay on waste form structure and the result from these calculations. Specifically, the focus is on the structural changes induced by the decay of $^{90}Sr^{2+}$ to $^{90}Zr^{4+}$. The response of a model Sr-containing material to changes in chemistry and charge was modeled with *ab initio* methods. The results of these simulations are compared to the results of the ion implantation experiments described above to validate the developed atomic-level models. This work supports modeling waste form structure at the atomistic level, provides insights for continuum level models, and enables the rational design of waste forms to mitigate the effects of chemical and charge imbalance.

Radionuclide decay in waste forms produces energetic beta particles, alpha particles, and gamma rays, as well as recoiling daughter products that are chemically different and whose change in ionic radius and valence state can significantly affect waste form structure. In the case of beta decay of the fission products ^{90}Sr and ^{137}Cs, substantial self-heating, chemical changes, and charge imbalance that can affect the structural stability of waste forms, leading to phase transformations and/or phase separation. In the work reported here, atomic-level models are developed that simulate these changes and are compared to experimental data for validation. The focus is on the decay of $^{90}Sr^{2+}$ to $^{90}Y^{3+}$ to $^{90}Zr^{4+}$, this document, and $^{137}Cs^{+}$ to $^{137}Ba^{2+}$, a later document, in model materials that can also be studied experimentally. In the longer term, models and experimental data may be provided for proposed waste forms. The general approach is:

- *Ab initio* calculations are to be used to study charge compensation, charge redistribution, and changes in bonding character. While somewhat more challenging because of the large change in charge, the initial work focused on the decay of $^{90}Sr^{2+}$ to $^{90}Zr^{4+}$ in a titanate model material. The variable valence state of Ti may serve to compensate for some of the charge imbalance (Vance et al. 1982).
- While the actual decay of $^{90}Sr^{2+}$ to $^{90}Zr^{4+}$ is challenging to study (Weber et al. 2009) it is possible to introduce similar charge imbalance by ion implantation. Thus, simulations are carried out under experimental conditions of introducing charge imbalance in model systems by ion implantation. Comparisons to experimental data serve to validate the models under these experimental conditions.

6. RESULTS AND DISCUSSION – THEORY

6.1 Material Model

For the study of $^{90}Sr^{2+}$ to $^{90}Zr^{4+}$, the selected material is strontium titanate ($SrTiO_3$, hereinafter STO) as a model surrogate waste form for ^{90}Sr. As a cubic crystal with a small unit cell, STO tractable for modeling with *ab initio* methods, and high-quality single-crystal subtracts are readily available for experimental purposes. The cubic structure of STO is shown in Figure 19.

Strontium titanate is a widely studied material, because of its cubic structure and interesting electrical properties (Tanaka et al. 2003). Many computational studies reported in the literature are focused on defects that affect electrical properties (Mackie et al. 2009), especially vacancy defects (Gentils et al. 2010; Keeble et al. 2010). In the work reported here, changes in properties such as conductivity are not of immediate interest. A literature search found little prior work on Zr in STO. A recent computational

study (Uberuaga et al. 2010) has been published of $Sr_{1-x}Zr_xTiO_3$ at higher Zr concentrations (x = 0.125, 0.25 and 1) representative of the later stages of $^{90}SrTiO_3$ waste form decay; the results of this study will be compared to theirs as appropriate.

6.2 Computational Approach

Calculations of minimum-energy atomic geometries, total energies and electronic states were carried out with density functional theory (DFT) in the Generalized Gradient Approximation (GGA) as described by Perdew, Burke and Enzerhof (1996) applied to a periodic supercell representation of STO.

The current results supply information only about thermodynamic stability in equilibrium; kinetic effects are left for future studies. The specific implementation of DFT used for the majority of the calculations was the periodic linear combination of atomic orbitals (LCAO) code QUEST (Feibelman 1986; Schultz 1999; Schultz 2000). SeqQuest contains norm-conserving pseudopotentials and high-quality contracted-Gaussian basis sets in a LCAO approach in its description of the electronic structure. SeqQuest has an implementation of the Local Moment Counter Charge (LMCC) method for the treatment of charged defects with reduced or eliminated finite-cell Coulomb effects. These capabilities are employed for the charged states of certain non-isovalent defects, for example Zr_{Sr}. This code is computationally very efficient, especially for relatively ionic compounds like STO. Relatively large basis sets and convergence criteria were used, such as to reduce computational errors in total energies to about 0.01 eV/atom. As a test, several calculations were repeated with the projector-augmented-wave DFT code VASP (Kresse and Furthmüller 1996; Kresse and Joubert 1999; Blöchl 1994), also with high precision settings, and results were in excellent agreement with QUEST.

6.3 Model Results

6.3.1 Phases of the Zr-Sr-Ti-O system

Reference calculations were carried out on all the competing phases likely to be important in the Zr-Sr-Ti-O system: O_2 gas; metallic Zr, Sr, and Ti; the oxides and suboxides SrO, TiO, Ti_2O_3, TiO_2 (rutile and anatase structures), ZrO_2 (monoclinic and cubic), and STO. Fictitious or hypothetical phases, such as ZrO with the rocksalt structure (same as SrO), $ZrTiO_3$, and $TiZrO_3$, were also considered, confirming that the latter were less stable than the expected phases. The lattice constants and atomic coordinates were fully relaxed to equilibrium in all cases, but only the enthalpy of formation and not the full free energy were

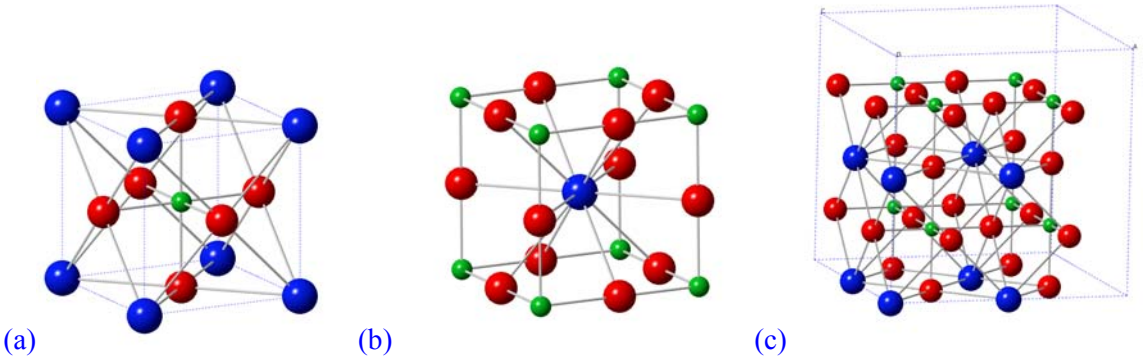

Figure 19. Room-temperature structure for the unit cell of $SrTiO_3$. Sr is blue, Ti is green, O is red. The structure is a perovskite oxide ABO_3. The Ti^{4+} ion is at the perovskite *B* site and has octahedral coordination, and the Sr^{2+} is at the *A* with twelve O nearest neighbors. Shown here are (a) Ti-centered, and (b) Sr-centered views of the unit cell; and (c) a 2 × 2 × 2 supercell, without replicated cell border atoms.

Table 2. Formation Enthalpy for relevant compounds in the Sr-Ti-Zr-O system. Experimental values from Chase (Chase 1998).

Compound	$-\Delta H_f$ (calc)(eV)	$-\Delta H_f$ (expt)(eV)
TiO	4.62	5.62
Ti_2O_3	14.48	15.76
TiO_2	9.20	9.73
ZrO	4.46	
ZrO_2	10.02	11.37
SrO	5.50	6.14
$SrTiO_3$	15.81	16.47
$ZrTiO_3$	11.73	
$TiZrO_3$	9.98	

calculated. The latter requires calculating the entropy at finite temperature, which requires the phonon spectrum; this may be treated in the future. The results confirmed published results for bulk STO and obtained bulk total energies for all the main alternative phases that might occur as composition within the Zr-Sr-Ti-O system is varied.

It is convenient to summarize our results for total energies in terms of the ground state enthalpy of formation, i.e. the energy difference between a compound and its constituent elements. The results are shown in Table 2 together with experimental values if known.

Several points can be made with the data shown in Table 2. The the formation enthalpy of Ti_2O_3 is slightly larger than the sum of the values for TiO and TiO_2, indicating that Ti_2O_3 is stable against decomposition into these two oxides. Likewise, $-\Delta H_f$ for TiO is slightly more than half that of TiO_2, indicating TiO is stable against decomposition into TiO_2 and Ti metal. On the other hand, the the formation energy of ZrO is less than half that of ZrO_2, indicating that ZrO will decompose into ZrO_2 and Zr metal, which is why ZrO is not observed. Strontium titanate will not decompose into SrO and TiO_2, but the metallic suboxides $ZrTiO_3$ and $TiZrO_3$ will decompose into TiO and ZrO_2. There is overall good agreement between theoretical and experimental values for the stable compounds.

6.3.2 Defect Studies

Defect studies were performed in STO with a $2 \times 2 \times 2$ and $3 \times 3 \times 3$ supercells. To test system size effects some defects were also treated in larger supercells. Calculations were carried out for Zr on Sr (Zr_{Sr}) and Ti (Zr_{Ti}) sites and the antisite defects Ti-on-Sr, and Sr-on-Ti symmetric neutral vacancies of Sr, Ti and O, and Sr, Ti, and Zr interstitials. To analyze the supercell size dependence of our results, the Zr_{Sr} impurity was investigated in $2 \times 2 \times 2$ (40 atom) and $3 \times 3 \times 3$ (135 atom) supercells of the simple cubic perovskite primitive lattice. A face-centered-cubic superlattice at $2 \times 2 \times 2$ (80 atoms), at $3 \times 3 \times 3$ (160 atoms), were also considered. The neutral defect energy converges fairly slowly with cell size, but is sufficiently converged for the purpose of this study at 135 atoms.

One goal is to predict the relative abundance of the most common point defects in crystalline Zr-doped STO, and these abundances are determined by the defect formation energy, defined as

$$\Delta E_{\text{defect}} = E_{\text{defect}} - E_{\text{ideal}} - \sum_i \Delta n_i \mu_i \qquad (1.3)$$

where E_{defect} is the total energy of a sufficiently large supercell containing the defect, E_{ideal} is the energy of an ideal supercell containing the same number of primitive unit cells, Δn_i is the number of atoms of element i added (or removed) to the ideal cell to produce the defect cell, and μ_i is the chemical potential

Table 3. Formation energies ΔE(eV) for various neutral defects, versus number of atoms in the ideal cell. The cell dimensions were held constant at the values derived from the computed bulk structure of STO (a = 3.949 Å), which was in close agreement with experiment (a = 3.905 Å) (Okazaki and Kawamina 1973).

Defect type	**Atoms**			
	40	**80**	**135**	**160**
$\mathbf{V_{Sr}}$	8.71(8.24)		8.41	
$\mathbf{V_{Ti}}$	14.58(14.62)		14.23	
$\mathbf{V_{O}}$	5.35(5.27)		4.44	
$\mathbf{O_{int}}$	1.75		1.41	
$\mathbf{Sr_{int}}$**(edge)**	7.64		6.09	
$\mathbf{Sr_{int}}$**(111 dumbbell)**			5.90	
$\mathbf{Ti_{int}}$ **(edge)**	4.52		3.54	
$\mathbf{Ti_{int}}$ **(111 dumbbell)**			4.22	
$\mathbf{Sr_{Ti}}$	10.13		8.92	
$\mathbf{Ti_{Sr}}$	5.43(5.41)		5.46	
$\mathbf{Zr_{Ti}}$	0.21		0.06	
$\mathbf{Zr_{Sr}}$	3.39(3.50)	3.11(3.23)	3.12(2.98)	2.66
$\mathbf{Zr_{int}}$ **(edge)**	6.68	5.52	5.51	5.05
$\mathbf{Zr_{int}}$ **(111 dumbbell)**	6.58	5.42	5.48	

for the ith element. The dependence on the chemical potentials reflects the free energy cost of supplying or removing the required number of atoms in an open system, and the concentration of the given defect is then proportional to $\exp(-\Delta H/kT)$ where T is the lowest absolute temperature at which the system was in thermal equilibrium. If E_i is the total energy per atom of an element in its pure bulk form, then a relative chemical potential is defined as

$$\mu_i^{\text{rel}} = \mu_i - E_i \tag{1.4}$$

The reference states for the element in STO were the pure metal crystals for Zr, Sr, and Ti, and half of the triplet O_2 molecule for oxygen.

Formation energies in eV for various neutral defects, versus number of atoms in the ideal cell, are shown in Table 3. Interstitials are tetragonal symmetric cell-edge centered, and a Sr-M (M=Sr,Ti,Zr) dumbbell oriented along the 111 direction. All others retain local cubic symmetry. The numbers in parenthesis are from the VASP code, all others are from the SeqQUEST code.

6.3.3 Native Defects

Native defects are those that involve only the material constituent atom vacancies, such as Sr, Ti, or O, in STO. The ambient population of native defects affects the behavior of interstitial and substitutional Zr. For example, the Zr donor is favored in natively p-type (metal poor) STO. Also, Zr_{Sr} or Zr_{inter} could form complexes with nearby host metal vacancies.

6.3.4 Substitutional Zr

The simplest case to consider for the end result of the ^{90}Sr to ^{90}Zr decay is a direct substitution of a Zr atom on a lattice site. Essentially, 1/8 of the Sr is replaced by Zr, if the Zr-on-Sr site impurity is modeled in the $2 \times 2 \times 2$ simulation cell. Of course, the concentration of Zr reached in actual waste as Sr decays would depend on the waste loading.

The possibility that the Zr_{Sr} substitutional defect might decay into two defects: Zr_{Ti} plus the antisite Ti_{Sr}, was considered, because Ti might have more of a tolerance than Zr for being less than fully ionized (Ti^{4+}

can be reduced to form Ti^{3+} or Ti^{2+} more easily than Zr^{4+}). However, Zr_{Sr} turned out to be stable by more than 2 eV against this reaction. It is energetically more favorable by about 2 eV per atom (a large amount) for Zr to remain on a Sr site. This is attributable to the significantly larger atomic radius of Zr than that of Ti. The Sr site has more volume available to accommodate a larger tetravalent ion, and this effect dominates. In other words, this high energy is from the steric hindrance to move the Zr from the Sr site. In addition, as stated in the experimental section, the expected recoil energy of the beta decay process is not sufficient to overcome the displacement threshold for Sr in STO, thus, Zr originating on a Sr lattice site through decay will remain there, assuming the STO crystal is otherwise unaltered.

6.3.5 Interstitial Zr, Sr, Ti, and O

The calculated interstitial defects are of particular interest because they may be expected to correlate to the Zr-implantation experiments. Direct Zr implantation will initially result in Zr interstitials. Knock-on effects will also then result in at least temporary interstitials of all available ion types. Two stable Zr interstitial configurations are found. One is a Sr-Zr-Sr edge site interstitial, in which the Zr is midway between two Sr atoms, and in the plane of the square formed by eight Ti and oxygen atoms. The adjacent Sr atoms are displaced away from the interstitial site. The second, lower energy interstitial configuration is a Zr-Sr dumbbell shape, or shared Sr-site/Zr-Sr interstitial, oriented along the <111> crystallographic direction of the unit cell. For both interstitials, the neighboring Ti atoms show minimal displacement. Investigation of the Sr and Ti ions found that they also have the same two types of stable configurations. The neutral and charged states (up to 4+ for Zr and Ti, up to 2+ for Sr) have similar geometry. ***The stable positions for the metal ion interstitials are consistent with the experimental results for the location of interstitials along the 100 and 111 directions, as shown by RBS data and McChasy simulation results, described in Section 3.2, and with PIXE results in Section 3.3 of the Experiment section of this report.***

The stability of the dumbbell configuration as compared to edge-site interstitial is enhanced as the system charge increases (becomes more positive). This result may have implications for the stability of the material to amorphization under irradiation. In pyrochlores (formula $A_2B_2O_7$), a stable dumbbell configuration has been shown to be associated with a greater likelihood of amorphization (Chartier et al. 2009). The atomic configurations of the interstitial configurations are shown in Figure 20.

Oxygen interstitials were also considered, for consistency with the oxygen impanation performed in the

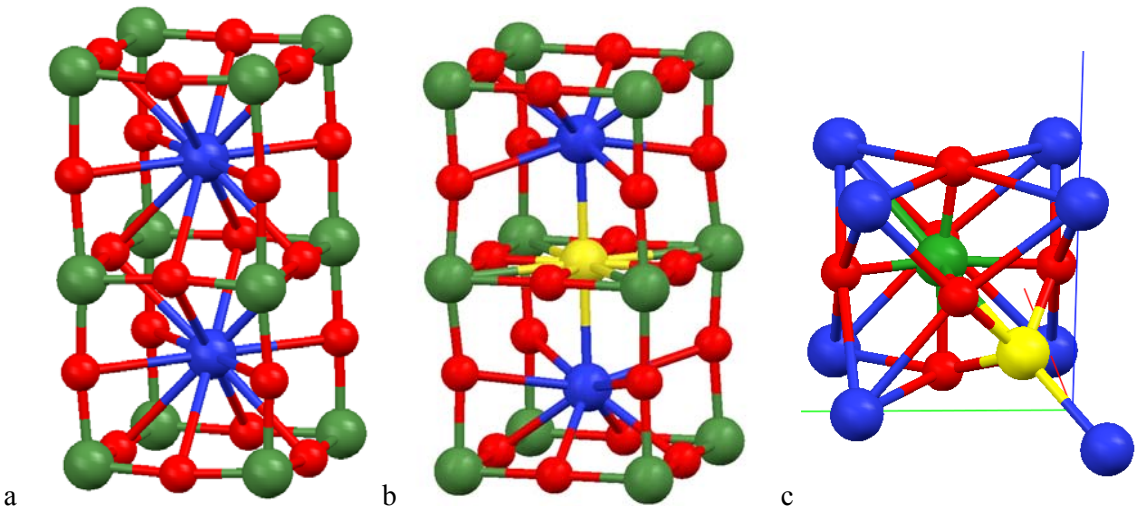

a b c

Figure 20. The optimized structure of the zirconium interstitials, as compared to the undistorted crystal structure. Strontium is blue, Ti is green, O is red, and Zr is yellow. (a) STO crystal; (b) edge-sharing interstitial site; (c) <111> Zr-Sr dumbbell interstitial site. Surrounding crystal cell atoms are omitted for clarity. The Sr and Ti interstitial configurations are similar to the Zr interstitals.

experiment. One stable configuration type was found, wherein the added oxygen inserts near a lattice oxygen, to form an O_2^{2-} dimer. This configuration is shown in Figure 21. This defect may be oriented along the <100>, <010>, or <001> direction.

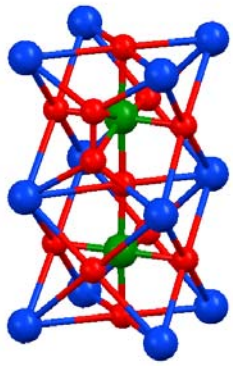

Figure 21. The optimized structure of the oxygen interstitial. An additional oxygen atom (red) is visible in the top half of the figure, such that there is an O-O dimer, where in the defect-free crystal there is only one O atom.

6.3.6 Swelling and structural distortion

The introduction of defects in a crystal results in changes in the optimal volume of the crystal. This is one measure that is possible to compare directly to experimental data. . Cell parameters were optimized for selected defect cases, shown in Table 4. As with the total energies, the volume changes per defect are fairly well converged with respect to supercell sizes at the 3 × 3 × 3 supercell.

The largest volume changes are for interstitials, where the volume increases by up to a few times the mean volume per atom of the bulk (about 12 Å^3). This is consistent with the notion of large compressive stress induced by placing an extra atom into a relatively close-packed structure such as perovskite. Substitutional Zr causes a smaller volume increase on the Ti site, consistent with Zr being slightly larger in atomic radius that the isovalent Ti atom, while Zr on a Sr site causes a small volume contraction, consistent with the large effective atomic radius of the alkaline earths. A Sr vacancy caused a lattice contraction, while the Ti vacancy caused a small expansion from weakened bonding interactions. The oxygen interstitial causes a smaller volume increase than the metal interstitials because it forms a close molecular dimer with a lattice oxygen ion. The results in the table are from a full relaxation of all unit cell parameters.

Relaxation of interstitial defect cells led to a minor tetragonal distortion along the direction of the defect, which is consistent with the experiment showing the formation of a minor tetragonal phase. Restriction of the relaxation to only the c axis, as is appropriate for comparison to the experiment, which shows that the new phase is epitaxially oriented with the host STO crystal, led to increased tetragonal distortion as compared to the unrestricted cells. The c/a ratio for the Zr interstitial was calculated to be 1.009. The experimental result, after annealing, is 1.007. This is good agreement within the limitation of DFT. The experimental results for XRD, GIXRD, MicroXRD, and HRXRD are discussed above in Section 3.4.

6.3.7 Effects of system charge

In an ionic solid like STO, defect ions are expected to be charged. The species present in the perfect

Table 4. Volume change in Å^3 per defect from allowing unit cell dimensions to relax, as a function of unit cell size. A small tetragonal distortion of the cell is also present for the interstitials.

Defect Type	**Atoms**		
	40	**80**	**135**
$\mathbf{V_{Sr}}$	–13.13		
$\mathbf{V_{Ti}}$	4.26		
$\mathbf{Zr_{int}}$**(edge)**	30.96	40.48	46.31
$\mathbf{Ti_{int}}$	23.28		
$\mathbf{Zr_{Sr}}$	–4.63		–4.07
$\mathbf{Zr_{Ti}}$	12.30		12.15
$\mathbf{O_{int}}$	7.53		8.27

crystal are essentially Sr^{2+}, Ti^{4+}, and O^{2-}. Therefore, it is necessary to consider charged states in order to accurately determine the relative stability of different defects. For a charged system the defect formation energy is defined as

$$\Delta E_f = E_T^{(def,q)} + E_T^{(perf)} - \sum_i \Delta n_i \mu_i - q\mu_e \quad (1.5)$$

$E_T^{(perf)}$, and $E_T^{(def,q)}$ are the total energies of the perfect crystal and the defect cell with charge q. The quantities Δn_i and μ_i are the change in the number of atoms of element i, and their chemical potential, as before. The quantity μ_e is the chemical potential of an electron in the perfect crystal, and $q = \Delta n_e$ or change in the number of electrons. The electron chemical potential can be related to the Fermi level of the crystal, and in practice can be difficult to define, or may have varying values, for these types of calculations (Hine et al. 2009).

Charged state calculations for the relevant charge states of each defect were performed on the 40 and 135 atom supercells. The theoretical investigation of charged defects in STO proved to be very challenging. None of the neutral or singly or doubly charged systems has localized defect states. The absence of a localized state means that it is impossible to calculate an ionization potential. Thus, it is impossible to rigorously determine the electron chemical potential and, thereby, report a charged state defect formation energy. The absence of localized defect states is a result that differs from a number of reported theoretical studies with DFT (Astala and Bristowe 2001a; Astala and Bristowe 2001b; Tanaka et al. 2003) but is consistent with others (Kim et al. 2009). Recent work indicates that quite large supersizes are required to represent charged defects in STO and, for the oxygen vacancy, the localized state seen in smaller calculations is increasingly shallow as the calculations increase in size (Buban et al. 2004). As the LMCC scheme is intended to represent the infinite limit and has been shown to converge more quickly with system size as compared to other methods, we believe our results are consistent with this observation. For more detailed descriptions of the electronic properties of STO, including charged defects, it would be considering other types of *ab initio* calculations, such as cluster based methods (Ricci et al. 2003) or LDA+U (Cuong et al. 2007). Such calculations are beyond the scope of this project at this time.

Table 5 summarizes the nature of the neutral and charged defects studied in STO. In the neutral state, the majority of the defects are either donors, with electrons in the conduction band, or acceptors, with unfilled levels below the valence band maximum. The oxygen interstitial is a shallow donor. The Zr substituted on a Ti site is neither a donor nor acceptor, as may be expected in substituting ions with the same preferred valence.

Although it is not possible at the present time to present absolute formations energies for the charged defects, it is possible to calculate energies that leave the electron chemical potential as an unknown quantity, such that the energy is expressed as a number +/-$N\varepsilon_F$, where N is the number of electrons added (or removed) to the system. Formation energies of charged defects calculated in this way are shown in Table 6. Note that the defect energy can then change with the Fermi level of the system.

With this data, it is possible to compare systems, or sets of systems, that have the same $N\varepsilon_F$. For example, a straightforward comparison is the change in relative stability of the <111> (dumbbell configuration) metal interstitials as compared to the <100> interstitials at each different charge level. This comparison is shown in Table 6. For each of the metal interstitials, the relative energy of <111> configuration drops as the charge becomes more positive. The data also shows that the $2 \times 2 \times 2$ is too small to have reached convergence, as the insertion of an ion along the <100> direction introduces more strain into the lattice than along the <111> direction.

Since the two possible interstitial sites are spatially quite close, the difference in energy for the two metal ion positions in their preferred oxidation state can be qualitatively related to their mobility through the STO lattice. The smaller the energy difference, the higher the ion mobility should be. From the data in Table 6, it is possible to surmise that Sr^{2+} ions should be considerably more mobile than Zr^{4+} ions. Conclusions cannot be made for Ti on this basis, as the higher charge state calculations did not fully converge. ***The (qualitative) greater mobility of Sr as compared to Zr is consistent with both results in the literature(Gomann et al. 2005), and with the current experimental results, as shown by SRIM, RBS, and McChasy before and after sample annealing, in Sections 3.1 and 3.2 of the Experiment Report.*** For more rigorous mobilities, calculations that find transition states are required. Such calculations are highly recommended for parameterization of larger time/length scale empirical model potential simulations of defect evolution.

6.3.8 Location of Zr in the lattice

For radioactive decay, the simple Zr_{Sr} is likely to occur since the decay energy and momentum of neither the initial decay to Y, nor the further decay to Zr exceed the threshold displacement energy required to move the atom from its initial lattice position.

However, the current experimental effort injects Zr into STO through implantation, so the simple Zr_{Sr} impurity will not be created initially. The goal is prediction of the most thermodynamically stable defect configurations for Zr in STO from the computed results, or the long-term fate of interstitial Zr.

6.3.8.1 Neutral systems

The most likely way to lower the energy of this defect is for Zr to replace a lattice atom, but that requires

Table 5. Identification of the nature of the highest occupied electronic state for relevant charge states of each defect. None of the defects studied had well-localized defect states. Labels are C= state is in the conduction band, V = state is in valence band, C(sh) = shallow level near conduction band minimum, V(sh) = shallow level near the valence band maximum. Labels in bold marked with an * indicate the preferred charge state for the defect.

	System Charge								
Defect Type	4^+	3^+	2^+	1^+	0 (neutral)	1^-	2^-	3^-	4^-
V_{Sr}	-	-	-	-	V	V	**V***		
V_{Ti}	-	-	-	-	V	V	V	**V**	**V***
V_O	-		**V(sh)**	C	C (sh)	C	-	-	-
O_{int}	-	-	V	V	**V(sh)***	C	C	-	-
Sr_{int}(edge)	-	-	**V***	C	C	-	-	-	-
Sr_{int}(111 dumbbell)	-	-	**V***	C(sh)	C	-	-	-	-
Ti_{int} (edge)	V*		C	C	C	-	-	-	-
Ti_{int} (111 dumbbell)			C	C	C	-	-	-	-
Sr_{Ti}					V				
Ti_{Sr}			**V***	C	C	-	-	-	-
Zr_{Ti}	-	-	-	V	**V***	C(sh)	C(sh)	C	-
Zr_{Sr}	-	-	**V***	C	C	-	-	-	-
Zr_{int} (edge)	**V***	C	C	C	C	-	-	-	-
Zr_{int} (111 dumbbell)	**V***	C	C	C	C	-	-	-	-

creating a native interstitial, i.e. Ti_{int} or Sr_{int}. For neutral symmetric defects, the resulting formation energy changes are (for $3 \times 3 \times 3$ supercells)

$$\begin{aligned} Zr_{int} &\rightarrow Zr_{Sr} + Sr_{int}, \quad \Delta H = 3.71\ \text{eV} \\ Zr_{int} &\rightarrow Zr_{Ti} + Ti_{int}, \quad \Delta H = -1.81\ \text{eV} \end{aligned} \tag{1.6}$$

or

$$Zr_{Sr} + Sr_{int} \rightarrow Zr_{Ti} + Ti_{int}, \quad \Delta H = 5.52\ \text{eV} \tag{1.7}$$

It is clear that Zr will not replace Sr at its normal lattice site under these conditions, but will spontaneously replace Ti, producing an interstitial Ti. This conclusion is not affected by the chemical potentials for the elements involved, since the reactions do not change the atomic composition of the system.

Next, consider the case where both a strontium vacancy and a zirconium interstitial are present. Obviously the system can lower its energy a great deal by recombining the Zr with the vacancy:

$$V_{Sr} + Zr_{int} \rightarrow Zr_{Sr}, \quad \Delta H = -10.77\ \text{eV} \tag{1.8}$$

Table 6. Formation energies ΔE(eV) for relevant neutral and charged defects in the 135 atom system. The cell dimensions were held constant at the values derived from the computed bulk structure of STO (a = 3.949 Å).

Vacancies		Sr and Ti Interstitials		Zr defects	
Defects	ΔE_f	**Defects**	ΔE_f	**Defects**	ΔE_f
V_{Sr}^{-}	2.68 - ε_F	$Sr_{int}(100)^{0}$	5.90	Zr_{Ti}^{0}	0.06
V_{Sr}^{2-}	-0.97 - $2\varepsilon_F$	$Sr_{int}(100)^{+}$	11.97 + ε_F		
		$Sr_{int}(100)^{2+}$	20.03 + $2\varepsilon_F$	Zr_{Sr}^{0}	3.03
V_{Ti}^{-}	8.3 - ε_F			Zr_{Sr}^{+}	8.90 + ε_F
V_{Ti}^{2-}	4.67 - $2\varepsilon_F$	$Sr_{int}(111)^{0}$	6.09	Zr_{Sr}^{2+}	16.90 + $2\varepsilon_F$
V_{Ti}^{4-}	4.10 - $4\varepsilon_F$	$Sr_{int}(111)^{+}$	11.75 + ε_F		
		$Sr_{int}(111)^{2+}$	19.84 + $2\varepsilon_F$	$Zr_{int}(100)^{0}$	5.51
V_{O}^{+}	10.33 + ε_F			$Zr_{int}(100)^{+}$	11.37 + ε_F
V_{O}^{2+}	18.29 + $2\varepsilon_F$	$Ti_{int}(100)^{0}$	3.54	$Zr_{int}(100)^{2+}$	19.4 + $2\varepsilon_F$
		$Ti_{int}(100)^{+}$	9.42 + $2\varepsilon_F$	$Zr_{int}(100)^{4+}$	42.8 + $4\varepsilon_F$
		$Ti_{int}(100)^{2+}$	17.5 + $2\varepsilon_F$		
O Interstital					
Defects	ΔE_f	$Ti_{int}(100)^{3+}$	27.8 + $3\varepsilon_F$		
O_{int}^{0}	1.41	$Ti_{int}(100)^{4+}$	41.2 + $4\varepsilon_F$	$Zr_{int}(111)^{0}$	5.48
O_{int}^{+}	9.3 + ε_F			$Zr_{int}(111)^{+}$	11.2 + ε_F
O_{int}^{2+}	19.4 + $2\varepsilon_F$	$Ti_{int}(111)^{0}$	4.2	$Zr_{int}(111)^{2+}$	19.15 + $2\varepsilon_F$
O_{int}^{-}	-2.37 - ε_F	$Ti_{int}(111)^{3+}$	28.5 + $3\varepsilon_F$	$Zr_{int}(111)^{4+}$	41.9 + $4\varepsilon_F$
O_{int}^{2-}	-4.00 - ε_F	$Ti_{int}(111)^{4+}$	41.4 (unconv)+ $4\varepsilon_F$		

for neutral defects (3 × 3 × 3 cell).

The main alternative would be for Zr to displace a Ti atom that then occupies the Sr vacancy. However, the formation energy to accomplish this is higher than for the Zr_{Sr} substitution by

$$Zr_{Sr} \rightarrow Zr_{Ti} + Ti_{Sr}, \quad \Delta H = 2.25 \text{ eV} \tag{1.9}$$

Thus, considering only neutral systems, Zr_{Sr} is stable despite the much lower formation energy of Zr_{Ti}, because reaction (1.9) requires the formation of the additional defect Ti_{Sr} which is quite high in energy, see Table 3 (135 atom cells). Thus, we predict that in thermal equilibrium, neutral Zr added to the STO lattice will replace a Ti at a regular lattice site, creating a Ti interstitial atom, while Zr replacing Sr will simply occupy the lattice site of the missing Sr. Both defects are donors (double for Zr_{Sr} and quadruple for Ti_{int}) with the excess electrons essentially at the STO conduction band minimum (CBM).

6.3.8.2 Charged systems

Since the separated vacancies and interstitials can lower their energy by transferring electrons, it is necessary to examine charged states. As stated above, although it is impossible to rigorously compute the formation energy of the individual charged defects form the results obtained here, it can be relevant to compare the relative sum of energy of combined systems with the same overall charge and composition. Thus, it is possible gain insight into the relative stability of the defects in the preferred charge state. This approach has been successfully applied for the determination of the relative formation energy of the charged and neutral oxygen vacancy in STO (Astala and Bristowe 2001b).

The Zr interstitial can lower its energy without moving by transferring two electrons from the Zr_{int} donor levels (effectively the CBM) to the Sr vacancy acceptor levels. With the values from the charged state calculations (Table 6), the Equation (1.8) becomes

$$V_{Sr}^{2-} + Zr_{\text{int}}^{2+} \rightarrow Zr_{Sr}^{0}, \quad \Delta H = -15.15 \tag{1.10}$$

so that the occupation of a Sr site become even more favored. However, the Zr_{Sr}^{0} defect is still a double electron donor, so it is necessary to take this one step further.

In the present case, for positively charged systems, it is possible to compare the relative energy of sums of systems with the same overall charge state. Using the calculated results for the preferred charge state of each defect, Equation (1.7) becomes

$$Zr_{Sr}(2^+) + Sr_{\text{int}}(2^+) \rightarrow Zr_{Ti}(0) + Ti_{\text{int}}(4^+), \quad \Delta H = -4.2 \text{ eV} \tag{1.11}$$

This assumes that 2 electrons are donated to some part non-local part of the crystal.
This result is consistent with the experimental finding that the Zr substitutes for Sr in the STO lattice, and not for Ti, as shown through the high-resolution HAADF TEM images in Section 3.3.

A suggested path toward more rigorous solutions is to perform larger *ab inito* calculations containing both defects to allow defect charge compensation within a single supercell. This type of calculation, with multiple charged defects, is not possible in the current implementation of the LMCC method, so the cell size required for convergence, using more conventional methods, would be considerable. That type of large calculation was beyond the reach of the current project, but should be considered for future work.

6.3.9 Charge compensation of Zr ions in STO

In the real-world STO system, the excess electrons from a substitional Zr will be compensated by acceptor defects or the reduction of a variable charge state ion (such as Fe). In the absence of a compensating defect, the Zr on a Sr site will donate two electrons to the conduction band of STO. Examination of the total and partial densities of states, as shown in Figure 22, indicates that the excess electron have Ti3d orbital character, indicating that Ti ions may be reduced. Bader charge analysis confirms that the net result is the slight reduction of Ti atoms in the STO lattice. This result is consistent with Cuong et al (2007). This leads to the conclusion that the valence change associated with Sr to Zr conversion results in the reduction of the oxidation state of lattice Ti. Fortunately, Ti is stable in both +3 and +2 oxidation states, as illustrated by the existence of the suboxides Ti_2O_3 and TiO, while Zr is not. The suboxide, ZrO, has never been reported, and calculations predict it to be thermodynamically unstable to decomposition into ZrO_2 and Zr metal. These observations suggest that the STO structure may be stabilized with respect to radioactive decay of Sr into Zr by the ability of a nonradioactive constituent (Ti in this case) to exist in lower oxidation states than it has in the parent compound. The conduction electrons are, as expected, delocalized over the entire simulation cell, so that every atom is affected, and the total change in charge on an individual atom is small. Attempts to localize the reducing effect through introduction of distortions in the Ti sublattice did not succeed, but further efforts in this area are of interest.

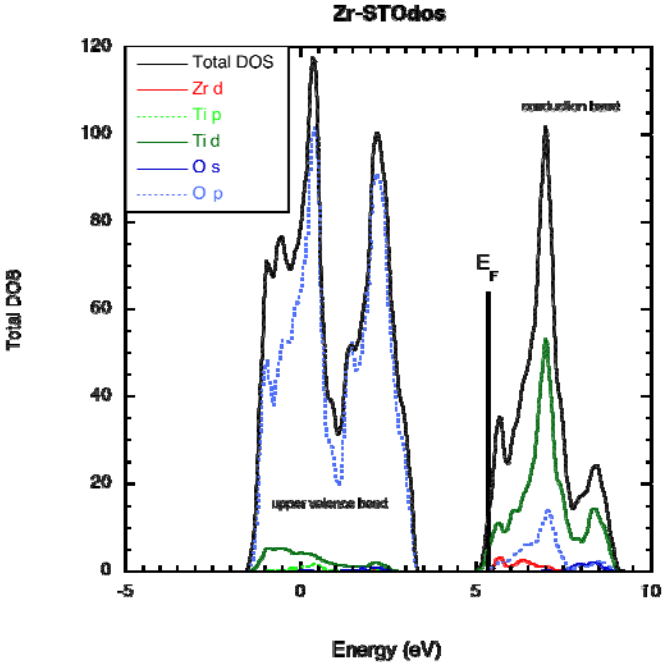

Figure 22. Total and partial densities of states for the supercell with composition $ZrSr_{15}Ti_{16}O_{48}$ (Zr on Sr site.) The Fermi energy (highest occupied level, with doping) lies below the Zr donor band (red) showing that the excess electrons are all in conduction-band states having mostly Ti 3d character. In the large-cell limit the Fermi energy goes to the conduction band edge, and the donor band becomes a discrete level. However, even in the supercell limit the donor is fully degenerate with the conduction band.

7. DISCUSSION – THEORY

The integrity of large encapsulated waste samples might be compromised by volume changes, even if only a fraction of the Sr has been converted into Zr. This considers changes resulting from the chemical transmutation of the elements themselves, and not from damage effects like the formation of voids or dislocation loops that may anneal or collapse over time. At sufficiently high concentrations, the predicted volume change of about +35 $Å^3$ per Zr for Zr_{Ti} + Ti_{int} (or Zr_{int}) would clearly destabilize a heavily Zr-implanted STO crystal. We expect radioactive decay of Sr to ultimately produce mainly Zr_{Sr} which is somewhat less disruptive to the lattice, with a volume change of about –4 $Å^3$ per Zr, but in the limit of a fictitious perovskite $ZrTiO_3$ this would still suggest a volume contraction of 6.5% relative to STO. In fact, we did a direct calculation of the equilibrium volume of "ZTO" and found it to be 6.4% smaller than the volume of STO, in close agreement with the above extrapolation. However, we found ZTO to be thermodynamically unstable against decomposition into TiO and ZrO_2, which together would have a volume change of –8.5% relative to the same number of moles of STO. We note that Uberuaga (2010) also found ZTO to be unstable against decomposition to ZrO_2, TiO_2 and Ti metal, though actually the

suboxide TiO is a more likely end form for all the titanium, since the reaction $2TiO \rightarrow Ti(metal) + TiO_2$ is slightly endothermic.

8. CONCLUSIONS

8.1 Experimental

There is no evidence showing a long-range diffusion of the implanted Zr in STO during the ion implantation at 550 K or thermal annealing up to 1423 K for 10 hours, which is in a sharp contrast to mobile Sr interstitials. Tight chemical bonding of Zr in the structure is expected. Significant lattice disorder in STO is observed after Implantation 1, but the material is not fully amorphized over the entire implanted region. The structure remains crystalline even after tripling the dose to 1.5 at% for Zr and O each in Implantation 2. Thermal annealing at 1273 K leads to a significant defect recovery at the surface, where the damage level is low and the implant concentration is negligible. However, complete recovery does not occur. At the damage peak, there is only a modest defect recovery after further annealing at 1423 K. Formation of defect clusters and presence of Zr implants in the depth region could be responsible for the hardness of defect recovery. The blocking ratio of Zr in STO after Implantation 2, as observed along the <001> axis, is estimated to be ~40% for annealing at 1273 K and ~50% for annealing at 1423 K. Nearly all the implanted Zr species are not located exactly at the original lattice sites in perfect STO due to lattice expansion. The co-implanted O as charge compensating ions in STO could play a role in the formation of the atomic configurations. In the damage layer, there is a high density of dislocations, Zr-containing structures and voids or oxygen blisters of a few nanometers in size. The Zr-containing structure is a superlattice structure with Zr substituting for Sr in STO at every other lattice site. Larger voids and dislocation loops also appear beyond the damage layer, which is likely a result of interstitial and vacancy diffusion.

As a result of crystal distortion in the damage layer, a tetragonal phase with $a = 0.3905$ nm and $c = 0.3968$ nm, having the c axis parallel to that of the STO ($a = c = 0.3905$ nm) substrate, is observed after Implantation 2 and annealing at 1273 K. This corresponds to a lattice expansion of ~1.6% along the normal of the free surface. The minor phase does not undergo substantial restructuring even after thermal annealing at 1423 K for 10 hours in Ar gas environments. After relaxation, lattice parameter c decreased to 0.3933 nm, corresponding to lattice shrinkage of only 0.9% along the c axis. New chemical bonding or a change in charge state was not observed because of the relatively thin layer and the large background of STO, which limit the detection sensitivity. Further experimental efforts are needed to study the atomic configurations of the Zr-containing structure.

8.2 Theory

Our calculations predict that in thermodynamic equilibrium, when considering neutral states, Zr added to the STO lattice will replace Ti at its regular lattice site, creating a Ti interstitials and Zr_{Ti} impurities, while calculations that make use of charged states show that Zr will displace Sr, creating Sr interstitials and Zr_{Sr} impurities. Zirconium replacing Sr (as in beta decay of Sr^{90}) will simply occupy the lattice sites of the missing Sr. Both Zr_{Sr} and Ti impurities are electronic donors, and both will strain the crystal lattice significantly, and eventually destabilize it at sufficiently high concentrations. Experiments reveal a change in lattice constants with Zr implantation of the same sign and roughly the same order of magnitude as our predictions. The chemical stability of Ti in reduced oxidation states contributes to the stability of donor-doped STO, and may hint at a broader strategy (use of multivalent constituents) to enhance the stability of fission product waste forms. The orientation and location of interstitial metal ions is also consistent with experimental data.

The structure of the possible new material (Section 3.3), with substitution of Zr at alternating Sr sites is an exciting result, and should be studied further. Modeling of this system would require a unit cell twice the size of the STO cell, and thus was not attempted at this time.

9. ACKNOWLEDGMENT

This work was supported by Nuclear Energy Research & Development, U.S. Department of Energy under Contract DE-AC05-76RL01830. The research was performed using EMSL, a national scientific user facility sponsored by the Department of Energy's Office of Biological and Environmental Research and located at Pacific Northwest National Laboratory. McChasy simulation study was financed by research grant from Polish Ministry of Science and Higher Education under number 714/N-EMSL/2010/0.

10. References

Astala, R, and PD Bristowe. 2001a. "Ab Initio and Classical Simulations of Defects in $SrTiO_3$." *Computational Materials Science* 22:81-86.

Astala, RK, and PD Bristowe. 2001b. "Ab Initio Study of the Oxygen Vacancy in $SrTiO_3$ " *Modelling Simul. Mater. Sci. Eng.* 9:415-22.

Blöchl, PE. 1994. "Projector Augmented-Wave Method." *Physical Review B* 50:17953.

Buban, JP, H Iddir, and S Ogut. 2004. "Structural and Electronic Properties of Oxygen Vacancies in Cubic and Antiferrodistortive Phases of $SrTiO_3$." *PHYSICAL REVIEW B* 69:180102(R).

Chartier, A, G Catillon, and J-P Crocombette. 2009. "Key Role of the Cation Interstitial Structure in the Radiation Resistance of Pyrochlores." *PHYSICAL REVIEW LETTERS* 102. 10.1103/PhysRevLett.102.155503.

Chase, MW, Jr. 1998. "NIST-JANAF Thermochemical Tables, 4th Edition." *J. Phys. Chem.* (Reference Data Monograph 9).

Cherniak, D. 1993. "Lead Diffusion in Titanate and Preliminary Results on the Effects of Radiation Damage on Pb Transport." *Chemical Geology* 110:177-94.

Chu, W, JW Mayer, and MA Nicolet. 1978. *Backscattering Spectrometry*. Academic press, San Diego.

Cooper, R, K Smith, M Colella, E Vance, and M Phillips. 2001. "Optical Emission Due to Ionic Displacements in Alkaline Earth Titanates." *Journal of Nuclear Materials* 289:199-203.

Cuong, DD, B Lee, KM Choi, H Ahn, S Han, and J Lee. 2007. "Oxygen Vacancy Clustering and Electron Localization in Oxygen-Deficient $SrTiO_3$: Lda+U Study." *Physical Review Letters* 98:115503.

Feibelman, PJ. 1986. "Efficient Solution of Poisson's Equation in Linear Combination of Atomic Orbitals Calculations of Crystal Electronic Structure." *PHYSICAL REVIEW B* 33:719.

Feldman, L, J Mayer, and S Picraux. 1982. *Materials Analysis by Ion Channeling*. Academic Press, New York.

Fromknecht, R, I Khubeis, and O Meyer. 2000. "Tin Implanted in Rutile Single-Crystal: Lattice Location, Diffusion and Precipitation." *Nuclear Instruments and Methods in Physics Research B* 166-167:322-28.

Gentils, A, O Copie, G Herranz, F Fortuna, M Bibes, K Bouzehouane, É Jacquet, C Carrétéro, M Basletić, E Tafra, A Hamzić, and A Barthélémy. 2010. "Point Defect Distribution in High-Mobility Conductive $SrTiO_3$ Crystals." *PHYSICAL REVIEW B* 81:144109. 10.1103/PhysRevB.81.144109

Gomann, K, G Borchardt, M Schulz, A Gomann, W Maus-Friedrichs, B Lesage, O Kaitasov, S Hoffman-Eifert, and T Schneller. 2005. "Sr Diffusion in Undoped and La-Doped $SrTiO_3$ Single Crystals under Oxidizing Conditions." *Physical Chemistry Chemical Physics* 7(9):2053-60.

Hine, NDM, K Frensch, WMC Foulkes, and MW Finnis. 2009. "Supercell Size Scaling of Density Functional Theory Formation Energies of Charged Defects." *Physical Revew B* 79:024112.

Jiang, C, CR Stanek, NA Marks, KE Sickafus, and BP Uberuaga. 2010. "Radioparagenesis: The Formation of Novel Compounds and Crystalline Structures Via Radioactive Decays." *Philosophical Magazine Letters* 90:435-46.

Jiang, W, ME Bowden, Z Zhu, P Jozwik, J Jagielski, and A Stonert. 2011. "Defects and Minor Phases in O^+ and Zr^+ Ion Co-Implanted $SrTiO_3$." *Industrial & Engineering Chemistry Research* submitted.

Jiang, W, P Nachimuthu, WJ Weber, and L Ginzbursky. 2007. "Variation in Lattice Parameters of 6H-SiC Irradiated to Extremely Low Doses." *Applied Physics Letters* 91:091918.

Jiang, W, WJ Weber, L Lian, and N Kalkhoran. 2009. "Disorder Accumulation and Recovery in Gold-Ion Irradiated 3C-SiC." *Journal of Applied Physics* 105:013529.

Jiang, WaWW. 2001. "Multiaxial Channeling Study of Disorder Accumulation and Recovery in Gold-Irradiated 6H-SiC." *Physical Review B* 64:125206.

Keeble, DJ, RA Mackie, W Egger, B Löwe, P P., H C., and TJ Jackson. 2010. "Identification of Vacancy Defects in a Thin film Perovskite Oxide." *Physical Review B* 81. 10.1103/PhysRevB.81.064102

Kim, YS, J Kim, SJ Moon, WS Choi, YJ Chang, J-G Yoon, J. Yu, J-S Chung, and TW Noh. 2009. "Localized Electronic States Induced by Defects and Possible Origin of Ferroelectricity in Strontium Titanate Thin films " *Applied Physics Letters* 94:202906.

Kresse, G, and J Furthmüller. 1996. "Efficiency of Ab-Initio Total Energy Calculations for Metals and Semiconductors Using a Plane-Wave Basis Set." *Comput. Mater. Sci.* 6:15.

Kresse, G, and J Joubert. 1999. "From Ultrasoft Pseudopotentials to the Projector Augmented-Wave Method." *Physical Review B* 59:1758.

Lide, DR. 2003. *Handbook of Chemistry and Physics*. CRC Press, Boca Raton, FL.

Mackie, RA, S Singh, J Laverock, SB Dugdale, and DJ Keeble. 2009. "Vacancy Defect Positron Lifetimes in Strontium Titanate." *Physical Revew B* 79: 014102. 10.1103/PhysRevB.79.014102.

Nilsen, WG, and JG Skinner. 1968. "Raman Spectrum of Strontium Titanate." *Journal of Chemical Physics* 48(5):2240-48.

Nowicki, L, A Turos, R Ratajczak, A Stonert, and F Garrido. 2005. "Modern Analysis of Ion Channeling Data by Monte Carlo Simulations." *Nuclear Instruments and Methods in Physics Research B* 240:277-82.

Okazaki, A, and M Kawamina. 1973. "Lattice-Constant of Strontium-Titanate at Low-Temperatures." *Materials Research Bulletin* 8(5):545-50.

Perdew, JP, K Burke, and M Ernzerhof. 1996. "Generalized Gradient Approximation Made Simple." *Physical Review Letters* 77:3865.

Ramos, S, B Canut, P Moretti, P Thevenard, and D Poker. 1995. "Thermal Evolution and Diffusion of Eu-Implanted $SrTiO_3$." *Thin Solid Films* 259:113-17.

Ricci, D, G Bano, and G Pacchioni. 2003. "Electronic Structure of a Neutral Oxygen Vacancy in $SrTiO_3$." *Physical Review B* 68(22):224105.

Sakaguchi, I, S Hishita, and H Haneda. 2001. "Diffusion and Aggregation of Si Implant in (100) Single-Crystal $SrTiO_3$." *Nuclear Instruments and Methods in Physics Research B* 173:436-40.

Schultz, PA. 2000. "Charged Local Defects in Extended Systems." *Physical Review Letters* 84:1942-45.

Schultz, PA. 1999. "Local Electrostatic Moments and Periodic Boundary Conditions." *Physical Review B* 60:1551.

Smith, K, M Colella, R Cooper, and E Vance. 2003. "Measured Displacement Energies of Oxygen Ions in Titanates and Zirconates." *Journal of Nuclear Materials* 321:19-28.

Smith, K, and N Zaluzec. 2005. "The Displacement Energies of Cations in Perovskite ($CaTiO_3$)." *Journal of Nuclear Materials* 336(2-3):261-66.

Tanaka, T, K Matsunaga, Y Ikuhara, and T Yamamoto. 2003. "First-Principles Study on Structures and Energetics of Intrinsic Vacancies in $SrTiO_3$ " *Physical Revew B* 68(20):205213. 10.1103/PhysRevB.68.205213.

Thevuthasan, WJ S, V Shutthanandan, and W Weber. 2003. "Accumulation of Ion Beam Induced Disorder in Strontium Titanate." *Nuclear Instruments and Methods in Physics Research B* 206:162-65.

Thevuthasan, S, C Peden, M Engelhard, D Baer, G Herman, W Jiang, Y Liang, and W Weber. 1999. " The Ion Beam Materials Analysis Laboratory at the Environmental Molecular Sciences Laboratory." *Nuclear Instruments and Methods in Physics Research A* 420(1-2):81-89.

Thomas, B, N Marks, and S Begg. 2007. "Defects and Threshold Displacement Energies in $SrTiO_3$ Perovskite Using Atomistic Computer Simulations." *Nuclear Instruments and Methods in Physics Research B* 245(2):211-18.

Tollefson, J. 2010. "Fuel and Waste No Bar to US Nuclear Growth." *Nature* 467:376-77.

Uberuaga, BP, C Jiang, CR Stanek, KE Sickafus, NA Marks, DJ Carter, and AL Rohl. 2010. "Implications of Transmutation on the Defect Chemistry in Crystalline Waste Forms." *Nuclear Instruments and Methods B* 268(19):3261.

Vance, ER, R Roy, JG Pepin, and DK Agrawal. 1982. "Chemical Mitigation of the Transmutation Problem in Crystalline Nuclear Waste Radiophases." *Journal of Material Science* 17(4):947-52.

Weber, WJ, A Navrotsky, S Stefanovsky, ER Vance, and E Vernaz. 2009. "Materials Science of High-Level Nuclear Waste Immobilization." *Materials Research Bulletin* 34(1):46-53.

Zhang, Y, F Gao, W Jiang, D McCready, and W Weber. 2004. "Damage Accumulation and Defect Relaxation in 4H-SiC." *Physical Review B* 70(12):125203.

Zhang, Y, J Lian, CM Wang, W Jiang, RC Ewing, and WJ Weber. 2005. "Ion-Induced Damage Accumulation and Electron-Beam-Enhanced Recrystallization in SrTiO3." *Physical Review B* 72(9). 09411210.1103/PhysRevB.72.094112.

Ziegler, J, J Biersack, and U Littmark. 1985. *The Stopping and Range of Ions in Solids*. Pergamon, New York.